J|A|C|S
ARTICLES

Elucidation of the Chiral Recognition Mechanism of Cinchona Alkaloid Carbamate-type Receptors for 3,5-Dinitrobenzoyl Amino Acids

Norbert M. Maier,[‡] Sabine Schefzick,[†] G. M. Lombardo,[†] Miguel Feliz,[§]
Kari Rissanen,[||] Wolfgang Lindner,[‡] and Kenny B. Lipkowitz*[,†]

Contribution from the Department of Chemistry, Indiana University-Purdue University at Indianapolis (IUPUI), 402 North Blackford Street, Indianapolis, Indiana 46202, Institute of Analytical Chemistry, University of Vienna, Währingerstrasse 38, A-1090 Vienna, Austria, Unitat de RMN d'Alt Camp, Serveis Cientificio Tècnics, Universitat de Barcelona, Marti i Franquès 1-11, E-08028 Barcelona, Spain, and Department of Chemistry, University of Jyväskylä, P.O. Box 35, FIN-40351, Jyväskylä, Finland

Received February 11, 2002

Abstract: A cinchona alkaloid having extraordinary chiral discriminatory powers ($\alpha = 32.6$ for dinitrobenzoyl leucine) is developed as a chiral stationary phase (CSP) for chromatography. An explanation of how chiral discrimination takes place is presented. Using a soluble analogue of the CSP, we found that NMR spectrometry indicates that 1:1 complexes exist for both optical isomers interacting with the CSP, that the free base form of the CSP exists in an open/closed ratio of 35/65 but that the protonated, bound-state form is exclusively in the anti-open conformation, and that significant intermolecular NOEs exist for the more stable diastereomeric complex but not for the less stable complex. Stochastic molecular dynamics simulations were carried out in solvents of low and high dielectric. The chromatographic retention orders and free energy differences of analyte binding to CSP were reproduced computationally as were the observed intra- and intermolecular NOEs. Data from the simulation were used to evaluate the intermolecular forces responsible for analyte binding as well as to discern fragments of the CSP doing most of the work of holding the complexes together. The enantiodifferentiating forces and the parts of the CSP most responsible for chiral discrimination are described. Moments of distributions of key dihedral angles and distances between centroids were used to assess the relative rigidity of the competing diastereomeric complexes. Simultaneous multiple-contact ion-pairing, hydrogen bonding, and π-stacking are possible for the longer retained enantiomer only. An X-ray crystallographic study of the more stable complex confirms the conclusions derived from chromatography, NMR spectroscopy, and molecular modeling.

Introduction

The economic importance of enantiomerically pure compounds has stimulated an active search for efficient asymmetric synthesis and enantioseparation strategies.[1,2] For the direct chromatographic resolution of enantiomers, chiral stationary phases (CSPs) comprising immobilized enantioselective receptors (chiral selectors, SOs) are firmly established.[3] The current trend of using CSPs for industrial scale production of enantiomers, however, defines new challenges for SOs including low costs, high chemical robustness, and broad solvent compatibility. A more important requirement, and one which is rarely observed in separation science, is a high level of target-specific enantioselectivity.[3]

Addressing these needs, our group has introduced novel SOs based on the cinchona carbamate motif.[4,5] These SOs show enantioseparation capabilities for a broad range of chiral acid analytes (selectands, SA) that are characterized by high versatility with respect to the fields of application. Thus, cinchona carbamate-type SOs have been employed for enantioseparation in liquid chromatography[4−6] and capillary electrochromatography,[7−9] as chiral background additives in capillary electrophoresis,[10] and as chiral carriers in liquid extraction separation.[11] During the course of these investigations, we were able to

---

* To whom correspondence should be addressed. E-mail: lipkowitz@chem.iupui.edu.

[†] Indiana University-Purdue University at Indianapolis.

[‡] University of Vienna.

[§] Universitat de Barcelona.

[||] University of Jyväskylä.

(1) Stinson, S. C. *Chem. Eng. News* **2001**, *79*, 45−56.

(2) Maier, N. M.; Franco, P.; Lindner, W. *J. Chromatogr., A* **2001**, *906*, 3−33.

(3) Francotte, E. R. *J. Chromatogr., A* **2001**, *906*, 379−397.

(4) Lämmerhofer, M.; Lindner, W. *J. Chromatogr., A* **1996**, *741*, 33−48.

(5) Lämmerhofer, M.; Maier, N. M.; Lindner, W. *Am. Lab.* **1998**, 71−78.

(6) Maier, N. M.; Nicoletti, L.; Lämmerhofer, M.; Lindner, W. *Chirality* **1999**, *11*, 522−528.

(7) Tobler, E.; Lämmerhofer, M.; Lindner, W. *J. Chromatogr., A* **2000**, *875*, 341−352.

(8) Lämmerhofer, M.; Peters, E. C.; Yu, C.; Svec, F.; Frechet, J. M. J.; Lindner, W. *Anal. Chem.* **2000**, *72*, 4614−4622.

(9) Lämmerhofer, M.; Svec, F.; Frechet, J. M. J.; Lindner, W. *Anal. Chem.* **2000**, *72*, 4623−4628.

(10) Lämmerhofer, M.; Zarbl, E.; Lindner, W. *J. Chromatogr., A* **2000**, *892*, 509−521.

(11) Kellner, K.-H.; Blasch, A.; Chemiel, H.; Lämmerhofer, M.; Lindner, W. *Chirality* **1997**, *9*, 268−273.

10.1021/ja020203i CCC: $22.00 © 2002 American Chemical Society

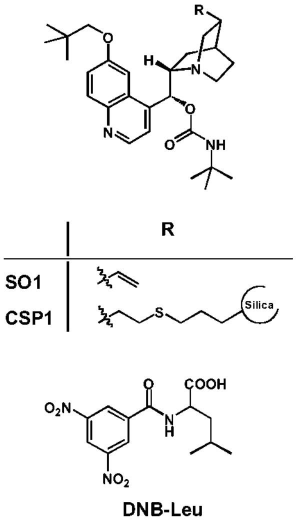

Figure 1. Chemical structures of the investigated cinchona alkaloid carbamate **SO1** and the respective chiral stationary phases **CSP1** and **DNB-Leu**.

achieve particularly high chromatographic enantioseparation factors ($\alpha > 10$) for *N*-3,5-dinitrobenzoyl amino acids with immobilized cinchona carbamates and mobile phases comprising buffered methanol−water mixtures. These "receptorial" levels of enantioselectivity in the presence of strongly competing polar/protic environments indicate the existence of highly efficient chiral recognition mechanisms for these SO−SA combinations. We feel that a detailed investigation of the stereodiscriminating pathways for these rare model systems may provide invaluable information on the nature of the intermolecular interaction forces as well as the cooperativity of those forces involved in the enantioselective association events. This knowledge may be instrumental for advancement of predictive recognition models for new classes of analytes and, more importantly, may serve as a guide for the rational design and optimization of the SOs by focused structural modifications.

In this contribution, we report the results of our efforts to elucidate the stereodiscriminating mechanisms for the enantiomers of 3,5-dinitrobenzoyl leucine (**DNB-Leu**) with 6-neopentoxy-9-*tert*-butylcarbamoyl cinchonidine **SO1** depicted in Figure 1. To provide a refined mechanistic picture for chiral recognition with this unusually efficient SO, we present here a detailed experimental and theoretical analysis of this highly enantiodiscriminating system.

Results and Discussion

Chromatographic Determination of the Differential Free Binding Energies $\Delta_{R,S}$ (ΔG). Energy-related measures for the stereodiscriminatory performance were established by liquid chromatography using an immobilized version of **SO1**. For this purpose, the quinine-derived receptor was attached covalently to mercaptopropyl-modified silica gel[6] to give the respective chiral stationary phase **CSP1**. This was packed into chromatographic columns and tested under HPLC conditions with racemic as well as enantiomerically enriched **DNB-Leu** using a hydro-organic buffered mobile phase. The chromatographic data revealed the enantioseparation factor $\alpha = 32.6$ for **CSP1** and the elution order with **(*S*)-DNB-Leu** being the more strongly retained enantiomer. From the α-value, the corresponding differential free energy of binding ($\Delta_{R,S}(\Delta G)$) was calculated according to $\Delta_{R,S}(\Delta G) = -RT \ln \alpha$ to give −8.63 kJ/mol for **CSP1** at 298 K.

It should be stressed that chromatographically established $\Delta_{R,S}(\Delta G)$ data represent good estimates for the intrinsic $\Delta_{R,S}(\Delta G)$ values of the respective diastereomeric complexes as long as nonselective retention increments and/or adverse immobilization effects can be neglected.[12−14] To probe the nonselective contributions to analyte retention, control experiments with a column packed with only the supporting mercaptopropylsilica were performed. **DNB-Leu** was found to be essentially nonretained on this material under the above mobile phase conditions. This confirms that nonselective retention effects are insignificant with **CSP1**. Moreover, we have demonstrated recently for a very similar receptor and **DNB-Leu** enantiomers an excellent agreement between chromatographic enantioselectivity and that derived in solution via microcalorimetry and CD spectroscopy.[15] This latter study rules out the possibility that the enantioselectivity of cinchona carbamates is significantly compromised by the employed immobilization chemistry. In light of this experimental evidence, it is justified to assume that the chromatographically established magnitude of enantioselectivity correlates well with the intrinsic $\Delta_{R,S}(\Delta G)$ values of the diastereomeric **SO1·DNB-Leu** complexes.

NMR Spectroscopy. ^{1}H NMR spectroscopy represents an ideal tool to study enantioselective association phenomena between molecules in solution,[16−23] giving access to a wealth of structure-related information. Thus, continuous variation-type NMR experiments allow one to establish the stoichiometry of transient diastereomeric complexes, and nuclear Overhauser enhancement (NOE) effects are sensitive probes that can be used to assess the spatial proximity between molecules or parts of molecules. Specifically, intramolecular NOEs are instrumental in determining the preferred conformations of molecules in the free, uncomplexed state and conformational changes that might occur upon SO−SA binding. Intermolecular NOEs give invaluable information about the time-averaged geometry of transient diastereomeric associates, and, in a complementary way, complexation-induced chemical shifts (CISs) of protons generally reflect local magnetic anisotropies induced by the proximity of specific functional groups of bound components.

In the following section, we will describe the results of our ^{1}H NMR investigations of diastereomeric complexes formed between the enantiomers of **DNB-Leu** and **SO1**, paying special attention to these intra- and intermolecular events. From an experimental viewpoint, aggregation phenomena, which are

---

(12) Schurig, V.; Juza, M. *J. Chromatogr., A* **1997**, *757*, 119−135.

(13) Fornstedt, T.; Sajonz, P.; Guiochon, G. *J. Am. Chem. Soc.* **1997**, *119*, 1254−1264.

(14) Fornstedt, T.; Götmar, G.; Andersson, M.; Guiochon, G. *J. Am. Chem. Soc.* **1999**, *121*, 1664−1774.

(15) Lah, J.; Maier, N. M.; Lindner, W.; Vesnaver, G. *J. Phys. Chem. B* **2001**, *105*, 1670−1678.

(16) Pirkle, W. H.; Pochapsky, T. C. *J. Am. Chem. Soc.* **1987**, *109*, 5975−5982.

(17) Pirkle, W. H.; Murray, P. G.; Rausch, D. J.; McKenna, S. T. *J. Org. Chem.* **1996**, *61*, 4769−4774.

(18) Pirkle, W. H.; Selness, S. R. *J. Org. Chem.* **1995**, *60*, 3253−3256.

(19) Lipkowitz, K. B.; Roghothama, S.; Yang, J. *J. Am. Chem. Soc.* **1992**, *114*, 1554−1562.

(20) Chankvetadze, B.; Endresz, G.; Schulte, G.; Bergenthal, D.; Blaschke, G. *J. Chromatogr., A* **1996**, *732*, 143−150.

(21) Chankvetadze, B.; Schulte, G.; Bergenthal, D.; Blaschke, G. *J. Chromatogr., A* **1998**, *798*, 315−323.

(22) Endresz, G.; Chankvetadze, B.; Bergenthal, D.; Blaschke, G. *J. Chromatogr., A* **1996**, *732*, 133−142.

(23) Yashima, E.; Yamamoto, C.; Okamoto, Y. *J. Am. Chem. Soc.* **1996**, *118*, 4036−4048.

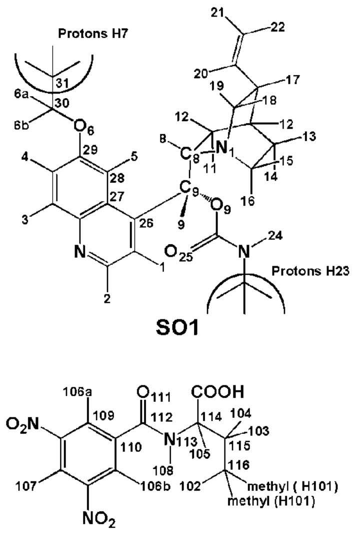

Figure 2. Atom numbering scheme of **SO1** and **DNB-Leu**.

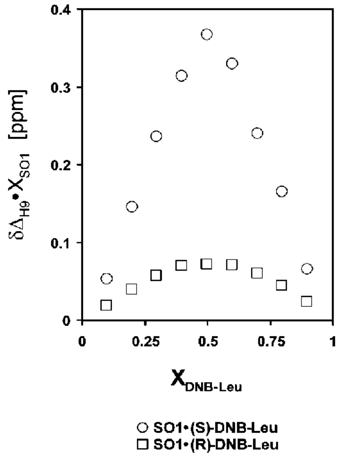

Figure 3. Job plot for the diastereomeric complexes **SO1·(*S*)-DNB-Leu** and **SO1·(*R*)-DNB-Leu**. Proton H$_9$ of **SO1** was used as the diagnostic proton, and the total concentration was 10 mM.

frequently observed with cinchona alkaloids and their derivatives, had to be considered. These effects, which can influence NMR data substantially, have been shown to be large at high levels of concentration and in apolar solvents.[24,25] To eliminate this potential source of complications, all experiments were thus performed with diluted samples (10 mM) and in methanol-d_4. The use of this solvent was also selected to generate medium conditions close to those employed in the chromatographic experiments. In the following discussions, we refer to individual protons of **SO1** and **DNB-Leu** according to the numbering scheme depicted in Figure 2.

Complexation Stoichiometry. To derive a detailed atomic level understanding of any molecular recognition process, a key element is to gain knowledge of the association stoichiometry of the interacting components. This is particularly crucial when studying multifunctional receptor systems, that may be prone to form higher order aggregates (see above). The binding stoichiometry between **SO1** and each enantiomer of **DNB-Leu** was established by continuous variation NMR titration protocols.[26−28] The chemical shift changes of the benzylic H$_9$ proton in **SO1** were recorded as a function of increasing concentrations of the individual **DNB-Leu** enantiomers as this resonance showed the most pronounced CIS. The corresponding Job plots are shown in Figure 3.

The maximum values for the relative complex concentrations were observed at **DNB-Leu** molfractions of 0.5, indicating clean 1:1 association stoichiometry for the more stable **SO1·(*S*)-DNB-Leu** as well as the less stable **SO1·(*R*)-DNB** complexes. These results suggest that the formation of the diastereomeric salt pairs involves only one and most probably the more strongly basic quinuclidine nitrogen of **SO1** rather than the quinoline nitrogen as an acceptor site.

Conformational Preferences of SO1. The stereodiscriminatory properties of cinchona alkaloids have been shown to be strongly associated with their conformational status. To evaluate this aspect in context with the chiral recognition system under investigation, we studied the conformational behavior of **SO1** in the free and complexed state. The conformational preferences of cinchona alkaloids and their derivatives have been thoroughly studied by spectroscopic and molecular modeling techniques.[25,29−33] The relative population of energy-allowed conformers depends on various parameters, including type and chemical nature of functional groups attached at the O$_9$-position, solvent polarity, protonation status, and participation of the quinuclidine nitrogen in complexation events. On the basis of molecular modeling studies, it has been established that cinchona alkaloids can adopt a number of energetically favorable closed and open type conformations.[29−32] In closed conformations, the lone pair of the quinuclidine nitrogen is directed toward the quinoline moiety, while for the open conformations, the lone pair points away from the aromatic substituent. However, for most cinchona alkaloids and their derivatives, only three specific conformers have been observed with ^{1}H NMR spectroscopy.[29,32]

In the following discussion, we show that these conformers also represent the physically relevant species for quinine carbamate derivatives. These conformers are depicted for the truncated **SO1** receptor (*tert*-butylcarbamoyl moiety omitted for clarity) in Figure 4a−c.

Note that a syn or anti subclassification is used to account for the relative orientation of C$_{29}$−O$_6$- and C$_9$−O$_9$-bonds to each other. Experimentally, we took advantage of specific inter-ring NOEs[29,31,32] detected by 2-D NOESY to establish the presence/absence of given conformations in the various investigated **SO1** species. The NOEs characteristic for the individual conformations are indicated in Figure 4a−c. We also considered the observed vicinal $^3J_{H_8H_9}$ coupling constants as another valuable diagnostic tool to gain information about the presence and relative population of specific conformations. Recently, Bürgi and Baiker[29] established reliable values for the H$_9$−C$_9$−C$_8$−H$_8$ dihedral angles of the individual anti-open, syn-closed, and

---

(24) Uccello-Barretta, G.; Bari, L. D.; Salvadori, P. *Magn. Reson. Chem.* **1992**, *30*, 1054−1063.

(25) Uccello-Barretta, G.; Balzano, F.; Quintavalli, C.; Salvadori, P. *J. Org. Chem.* **2000**, *65*, 596−3602.

(26) Job, P. *Ann. Chim.* **1928**, *9*, 113−134.

(27) Connors, K. A. *Binding Constants. The Measurement of Molecular Complex Stability*; Wiley: New York, 1987.

(28) Horner, J.; Perry, M. C. *J. Chem. Soc., Faraday Trans. 1* **1986**, *32*, 533−543.

(29) Bürgi, T.; Baiker, A. *J. Am. Chem. Soc.* **1998**, *120*, 12920−12926.

(30) Dijkstra, G. D. H.; Kellogg, R. M.; Wynberg, H.; Svendsen, J. S.; Marko, I.; Sharpless, K. B. *J. Am. Chem. Soc.* **1989**, *111*, 8069−8076.

(31) Dijkstra, G. D. H.; Kellogg, R. M.; Wynberg, H. *Recl. Trav. Chim. Pays-Bas* **1989**, *108*, 195−204.

(32) Dijkstra, G. D. H.; Kellogg, R. M.; Wynberg, H. *J. Org. Chem.* **1990**, *55*, 6121−6131.

(33) Berg, U.; Aune, M.; Matsson, O. *Tetrahedron Lett.* **1995**, *36*, 2137−2140.

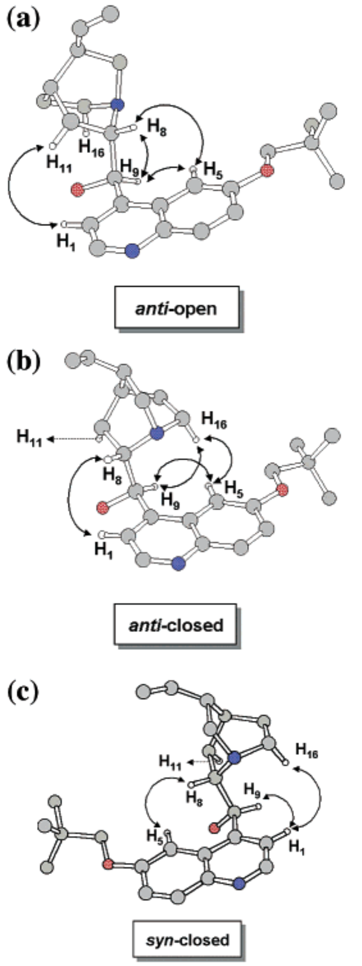

Figure 4. (a−c) Schematic representation of the physically relevant conformers of **SO1** with their characteristic inter-ring NOEs. Note that other protons and the O9-*tert*-butylcarbamoyl group of **SO1** are omitted for clarity.

anti-closed conformers of cinchonidine. Applying a modified Karplus equation, they calculated values for $^3J_{H_8H_9}$ to be 1.7, 9.6, and 9.4 Hz, respectively, for anti-open, syn-closed, and anti-closed alkaloid conformers. We will refer to these values for discussion of the conformational preferences of the various **SO1** species studied.

For the free base of **SO1**, a straightforward identification of the conformational situation was complicated by signal overlap of the diagnostic protons H_8 and H_{16}, leading to partially obscured NOESY cross-peaks. Fortunately, a NOE observed for H_1−H_{11} demonstrated the presence of the anti-open conformer, which was supported by a strong NOE between H_5 and H_9. An intense NOE between H_1 and H_8 provided evidence for the presence of the anti-closed and/or the syn-closed conformer. The value of 4.5 Hz for $^3J_{H_8H_9}$ suggested the anti-open conformer was the dominating species. Employing a known strategy to estimate the relative population of open versus closed conformers from the experimental $^3J_{H_8H_9}$ values[29] gave an open/closed ratio of 35/65. To establish the consequences of protonation on **SO1**, the corresponding **SO1·HCl** was also investigated. Strong H_1−H_{11}, H_5−H_9, and H_5−H_8 NOE signals were detected demonstrating the presence of the anti-open conformer. No NOE cross-peaks characteristic for any of the closed conformers were observed. The exclusive existence of the anti-open conformation was also corroborated by the small value for $^3J_{H_8H_9}$ (1.5 Hz), being in good agreement with the theoretically established value for the anti-open conformer. From this result, it is evident that protonation of **SO1** leads to a significant change in the conformational situation of **SO1**, strongly stabilizing the anti-open conformer. This observation is consonant with the behavior of other cinchona alkaloid derivatives.[30,32,34]

The investigation of the more stable diastereomeric **SO1·(*S*)-DNB-Leu** complex revealed a picture very similar to that found for **SO1·HCl**. Again, intensive H_1−H_{11}, H_5−H_9, and H_5−H_8 NOEs cross-peaks confirmed the dominating presence of the anti-open conformation, which was strongly supported by a vanishing $^3J_{H_8H_9}$. However, a significant dipolar interaction between H_9 and H_{16} was also detected, but no other NOE associated with any of the closed conformations. To rationalize this result, it can be assumed that binding of **(*S*)-DNB-Leu** to **SO1** generates a hybrid-type conformation displaying the structural features of both the anti-open and the anti-closed conformers. The energetic costs accompanied with this conformational change are compensated by stabilizing interactions established as a consequence of the intermolecular association with **(*S*)-DNB-Leu**. A similar complexation-induced conformational transition of a chiral recognition process has been observed for 9-*O*-(3,5-dimethoxyphenylcarbamoyl)-quinine recently.[25]

For the less stable diastereomeric **SO1·(*R*)-DNB-Leu** complex, a quite different scenario was observed. Besides dipolar interactions indicative for the anti-open conformer, NOEs characteristic for the coexistence of the syn-closed (H_1−H_9) and anti-closed (H_1−H_8) conformations were also present. In accordance with this observation was the larger value for $^3J_{H_8H_9}$ (3.0 Hz), corresponding to an open/closed ratio of 84/16. Hence, the conformational situation of **SO1** in the less stable diastereomeric complex represents an intermediate status between the free base and the more stable diastereomeric complex. In contrast to **(*S*)-DNB-Leu**, the (*R*)-enantiomer, at least when used at identical concentrations, fails to induce for **SO1** a complete transition to the anti-open conformation. This provides evidence that the conformational changes **SO1** is experiencing in the course of the complexation with **(*S*)-DNB-Leu** are definitely offset from an unspecific protonation effect, but such conformational changes must be assisted by additional intermolecular interactions.

Complexation-Induced Shifts. Chemical shift changes accompanying the association event were investigated to help establish the intermolecular interactions contributing to chiral recognition. Furthermore, it was anticipated that CISs would be instrumental in revealing some structural details with respect to the relative arrangement of the individual components in the diastereomeric complexes. For the system under investigation, it has to be considered that complexation, because of the acid−base nature of **DNB-Leu**/**SO1**, involves primarily ion-pair formation. Consequently, strong CISs associated with the protonation/deprotonation of the components may complicate the straightforward identification of CISs characteristic for additional, but crucial, nonionic intermolecular interactions.

To deconvolute these contributions, shift changes exclusively brought about by the protonation of **SO1** and deprotonation of **DNB-Leu** were evaluated separately. For this purpose, the chemical shifts of **SO1·HCl** and the sodium salt of **DNB-Leu**

---

(34) Ferri, D.; Bürgi, T.; Baiker, A. *J. Chem. Soc., Perkin Trans. 2* **1999**, 1305−1311.

Table 1. ^{1}H NMR Chemical Shifts (δ) of **SO1**, **SO1·HCl**, **DNB-Leu**, **DNB-Leu Sodium Salt**, and Complexation-Induced Shifts of **SO1·(*S*)-DNB-Leu** ($\Delta\delta_S$) and **SO1·(*R*)-DNB-Leu** ($\Delta\delta_R$), Respectively (For Numbering of Protons, see Figure 2)

H	δ^a (ppm)				$\Delta\delta^b$ (ppm)	
	SO1/ DNB-Leu	SO1·HCl/ DNB-Leu as sodium salt	SO1·(*S*)- DNB-Leu	SO1·(*R*)- DNB-Leu	$\Delta\delta_S$	$\Delta\delta_R$
1	7.53	7.68	7.46	7.55	−0.06	0.02
2	8.65	8.75	8.53	8.66	−0.11	0.02
3	7.96	8.03	7.62	7.95	−0.24	−0.01
4	7.45	7.58	7.08	7.46	−0.37	0.01
5	7.49	7.62	7.18	7.50	−0.31	0.01
6a,b	3.86	4.05	3.57	3.89	−0.29	0.03
7	1.11	1.13	1.12	1.12	0.01	0.01
8	3.23	3.80	3.62	3.65	0.39	0.42
9	6.47	6.93	7.49	6.73	1.02	0.26
10	1.66	1.82	1.63	1.76	−0.03	0.10
11	1.81	2.33	2.11	2.12	0.30	0.31
12	1.80	2.16	2.04	2.04	0.24	0.24
13	1.59	2.01	1.97	1.86	0.38	0.27
14	1.89	2.30	2.21	2.12	0.32	0.22
15	2.71	3.36	3.26	3.16	0.55	0.45
16	3.26	3.72	3.34	3.54	0.08	0.28
17	2.34	2.85	2.77	2.69	0.43	0.35
18	2.64	3.31	3.12	3.14	0.48	0.50
19	3.07	3.63	3.77	3.47	0.70	0.42
20	5.79	5.80	5.73	5.80	−0.06	0.01
21	4.93	5.06	4.99	5.02	0.06	0.09
22	4.97	5.14	5.08	5.10	0.11	0.13
23	1.26	1.27	1.45	1.27	0.19	0.01
24	n.d.^{c}	n.d.^{c}	n.d.^{c}	n.d.^{c}		
101	0.98	0.98	0.99	0.98	0.01	0
102	1.76	1.74	1.78	1.76	0.02	0
103, 104	1.85	1.77	1.87	1.82	0.02	−0.03
105	4.70	4.60	4.84	4.63	0.14	−0.07
106a,b	9.10	9.12	8.96	9.04	−0.14	−0.06
107	9.15	9.10	8.41	9.03	−0.74	−0.12
108	n.d.^{c}	n.d.^{c}	n.d.^{c}	n.d.^{c}		

[a] All spectra were recorded in methanol-d_4 at 298 K at a sample concentration of 10 mM. Chemical shifts referred to internal TMS. [b] Complexation-induced shifts are reported relative to the uncomplexed species. Negative signs denote upfield shifts. [c] Protons could not be detected.

were compared with those of the respective components in the free state. The corresponding chemical shifts are summarized in Table 1.

Evidently, the protonation of **SO1** induces deshielding for all protons. Substantial downfield shifts are observed for the protons of the quinuclidine moiety ($\Delta\delta = 0.4-0.6$), while the protons of the aromatic systems are less strongly affected ($\Delta\delta = 0.1-0.2$). The *tert*-butyl groups located at the O_6-neopentyl and O_9-carbamate substituents are almost unaffected. Again, these observations indicate that protonation of **SO1** occurs primarily at the more basic quinuclidine nitrogen. The CISs associated with the deprotonation of **DNB-Leu** were found to be less prominent. In the sodium salt of **DNB-Leu**, only the protons located directly at or close to the stereogenic center (H_{103}, H_{104}, and H_{105}) are shifted upfield moderately ($\Delta\delta \approx -0.1$).

With this guiding information in hand, attempts were made to identify and interpret structure-relevant CISs for diastereomeric complexes. For the more stable **SO1·(*S*)-DNB-Leu** diastereomer, a variety of specific CISs could be identified. For convenience of comparison, these CISs are summarized separately in Figure 5.

Concerning the quinuclidine portion of **SO1**, substantial downfield shifts of most of the protons reflect extensive protonation by the **(*S*)-DNB-Leu**. Within this set of protons, however, H_{16} and H_{19} show distinctly different behaviors as compared to the other quinuclidine protons. Relative to free **SO1** and **SO1·HCl**, H_{16} exhibits a surprisingly small downfield shift ($\Delta\delta = 0.08$), while H_{19} appears unusually strongly deshielded ($\Delta\delta = 0.70$). Considering the positions of H_{16} and H_{19} relative to the quinuclidine nitrogen, we found that the exceptional CISs of these protons are most probably caused by the ion-pairing carboxy group of **(*S*)-DNB-Leu**. More specifically, this observation suggests that these protons must be exposed to shielding and deshielding domains of the bound ligand, respectively. Another significant effect involves the aromatic protons of **SO1** which display upfield shifts in the presence of **(*S*)-DNB-Leu**, being most pronounced for H_3, H_4, and H_5 ($\Delta\delta = -0.34, -0.37$, and -0.31). The same is true for the $H_{6a,b}$ resonances of the O_6-neopentoxy group ($\Delta\delta = -0.29$), being located in close proximity to H_4 and H_5. In similar fashion, the aromatic protons of **(*S*)-DNB-Leu** also exhibit substantial upfield shifts ($\Delta\delta = -0.14$ and -0.74 for $H_{106a,b}$ and H_{107}, respectively). These pronounced mutual shielding effects provide compelling evidence for strong intermolecular face-to-face $\pi-\pi$ interactions between the aromatic groups.[16−18,35] The most pronounced CIS in the complex is detected for H_9, experiencing a downfield shift of $\Delta\delta = 1.02$. Although H_9 is deshielded on protonation (see δ-values for H_9 in **SO1** and **SO1·HCl** in Table 1 and Figure 5), protonation can only partly account for this dramatic shift. The spatial position of H_9 within the receptor suggests that this proton may come in contact with the deshielding region of the carboxylic group of **(*S*)-DNB-Leu** once it forms an ion pair with **SO1**. Alternatively, one can assume that subtle conformational changes enforced by complex formation (see above) may translocate H_9 into the deshielding domain of the quinoline ring or the carbamate carbonyl group. A feature unique for the **SO1·(*S*)-DNB-Leu** complex is the downfield CIS for the H_{23} protons of the *tert*-butyl carbamoyl group of **SO1** ($\Delta\delta = 0.19$). To rationalize this specific shift, we assume that the carbamate *tert*-butyl group is situated in a strongly deshielding region of **(*S*)-DNB-Leu** in the complexed state. Alternatively, the carbamate functionality may be engaged in some type of deshielding intermolecular interaction with **(*S*)-DNB-Leu**, most likely hydrogen bonding. Focusing on the **(*S*)-DNB-Leu** component of the complex, we found that CISs are dominated by the upfield shifts for the H_{106} and H_{107} protons, manifesting a deep involvement of its aromatic system in intermolecular $\pi-\pi$-stacking interactions (see above). Apart from this effect, a downfield CIS for H_{105} at the stereogenic center ($\Delta\delta = 0.14$) reflects deprotonation as a consequence of ion pairing with **SO1**. The protons of the isobutyl side chain (H_{101}, H_{102}, H_{103}, and H_{104}) appear practically unaffected, demonstrating their remote position from any shielding/deshielding functionalities of **SO1** in the complexed state.

In the less stable diastereomeric complex **SO1·(*R*)-DNB-Leu**, no specific CISs could be detected (see Table 1 and Figure 5) for either component. The upfield shifts of the quinuclidine protons relative to the free receptor are because of ion pairing, being also the prime interaction between **SO1** by **(*R*)-DNB-Leu**. In contrast to the more stable complex, the chemical shifts for the protons of the aromatic systems of **SO1** as well as of

---

(35) Heaton, N. J.; Bello, P.; Herradon, B.; Campo, A. d.; Jimenez-Barbero, J. *J. Am. Chem. Soc.* **1998**, *120*, 9632−9645.

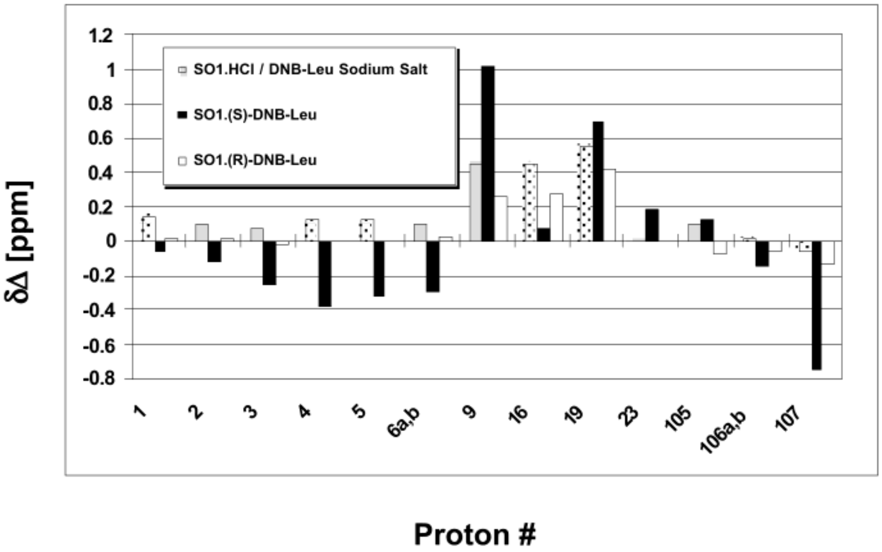

Figure 5. Complexation-induced chemical shifts for selected protons observed for **SO1·HCl**, **DNB-Leu sodium salt**, **SO1·(*S*)-DNB-Leu**, and **SO1·(*R*)-DNB-Leu** in methanol-d_4 at 298 K. The complexation-induced shifts are reported relative to free **SO1** and **DNB-Leu**, negative values denoting upfield shifts.

(*R*)-DNB-Leu appear almost unchanged relative to the free components. This finding suggests the inability of **(*R*)-DNB-Leu** to utilize intermolecular $\pi-\pi$-interaction for complex stabilization, a hypothesis that will later be proved by X-ray structure data and molecular modeling.

Intermolecular NOEs. To better establish the relative arrangement of the individual components of the transient **SO1·DNB-Leu** complexes, we attempted to detect close intermolecular contacts between the components by using 2-D NOESY techniques.[36] No intermolecular NOEs could be detected for the less stable **SO1·(*R*)-DNB-Leu**, an observation consistent with the aforementioned lack of CISs. In clear contrast, several close intermolecular contacts were evident for the more stable **SO1·(*S*)-DNB-Leu** associate. A weak but reproducible intermolecular NOE exists between $H_{6a,b}$ of the **SO1** and H_{105} of the **(*S*)-DNB-Leu**. Significantly stronger intermolecular NOEs are observable between the protons of the **(*S*)-DNB-Leu** isobutyl side chain (H_{101}, H_{102}, and H_{103}) and the H_{23} protons of the carbamate *tert*-butyl group of **SO1**. Additional intermolecular NOEs are observed between the aromatic $H_{106a,b}$ protons of **(*S*)-DNB-Leu** and the O6-neopentyl ($H_{6a,b}$, H_7) as well as the carbamate *tert*-butyl protons (H_{23}) of **SO1**. These results reveal that association between **SO1** and **(*R*)-DNB-Leu** is relatively inefficient and that binding does not take place at any specific "binding site" on **SO1**. The opposite seems to be true for the more stable complex. In this case, the intermolecular binding event is characterized by a high degree of spatial localization, allowing us to assign the time-averaged arrangement of **DNB-(*S*)-Leu** with respect to the O_6- and O_9-segments of **SO1**.

Association Model of SO1·(*S*)-DNB-Leu in Solution. Interpretation of the pooled experimental evidence collected by NMR spectroscopy for **SO1·(*S*)-DNB-Leu** allows us to advance a model for the time-averaged structure of this complex in solution. Intramolecular NOEs discussed above show that **SO1** in a complexed state adopts the anti-open conformation; structurally this implies that the spatially extended and bulky O_6-alkyl and O_9-carbamate groups take remote positions from each other, defining a shallow cleft for the selectand. At its center, the upper face of this cleft is occupied by the bulky quinuclidine moiety, providing the strongly basic acceptor site for protonation and eventual ion-pairing interaction with the analyte in its anionic form. Evidently, to approach this acceptor site, **(*S*)-DNB-Leu** must intercalate between the O_6-and O_9-substituents. The observed intermolecular NOEs indicate that this insertion process occurs in a stereochemically well-defined manner, placing the isobutyl side chain of **(*S*)-DNB-Leu** in close proximity to the carbamate *tert*-butyl group while aligning H_{105} toward the O_6-methylene group. Moreover, the aromatic portion of **(*S*)-DNB-Leu** takes a position allowing simultaneously for close contacts between its ortho protons and the O_6-neopentyl and carbamate *tert*-butyl group of **SO1**, respectively. Essentially, this specific docking mode orients the aromatic system of **(*S*)-DNB-Leu** in a parallel fashion to the lower face of the quinoline and thus generates an ideal spatial arrangement for intermolecular face-to-face $\pi-\pi$-stacking interactions as evidenced by NMR spectroscopy. The observation that **(*R*)-DNB-Leu** binds to **SO1** also via ion-pairing interactions, but fails to establish $\pi-\pi$-stacking interactions, demonstrates the restricted access to the binding site. The stereodiscrimination observed with **SO1** is obviously a consequence of simultaneous ion-pairing and $\pi-\pi$-stacking interactions, in combination with the pronounced shape selectivity of the binding domain.

X-ray Structure of the SO1·(*S*)-DNB-Leu Complex. Success in growing crystals of **SO1·(*S*)-DNB-Leu** allowed us to establish the solid-phase structure of the complex by single-crystal X-ray diffraction analysis. Strikingly, the complex in the solid-phase structure reflects, confirms, and rationalizes many of the structural details extracted from the results of the NMR spectroscopic investigations in solution. The corresponding structure is depicted in Figure 6.

In agreement with the NMR results, the **SO1** adopts an anti-open/syn-closed hybrid type conformation with internuclear distances of 2.16 Å (H_5, H_9), 2.48 Å (H_5, H_8), 2.64 Å (H_1, H_{11}),

---

(36) Neuhaus, D.; Williamson, M. *The Nuclear Overhauser Effect in Structural and Conformational Analysis*; VCH: Weinheim, 1989.

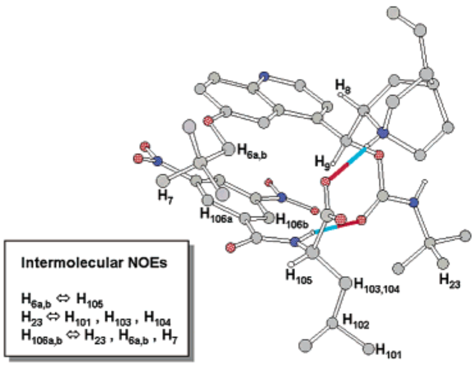

Figure 6. Ball-and-stick representation of the X-ray crystal structure of **SO1·(*S*)-DNB-Leu**. Intermolecular NOEs observed in methanol-d_4 (298 K, 10 mM) are indicated in the insert. Most protons are omitted for clarity.

and 2.85 Å (H_9, H_{16}). The O_6- and O_9-substituents attached at the cinchona skeleton are arranged to form a flat U-shaped cleft with a diameter of about 10 Å. The carbamate displays the energetically more favorable syn-orientation, having its carbonyl group located within the binding site. The O_6-methylene carbon is in-plane with the aromatic face of the quinoline, and its $H_{6a,b}$ protons are directed toward H_5, which also is consonant with their preferred orientation in solution established by an intramolecular NOE. As predicted by NMR results, **(*S*)-DNB-Leu** is located within this binding site forming via its carboxylic group a salt-bridge type hydrogen bond (O···H: 1.83 Å) with the quinuclidine nitrogen. Note that the quinuclidine proton H_{16} is located in close proximity (3.74 Å) and perpendicularly to the carboxylate group and resides 2.83 Å above the carbamate carbonyl function. Proton H_9 is found even closer to the carbamate carbonyl group (2.30 Å) and is eclipsed by H_{16}. This spatial arrangement appears to expose H_{16} and H_9 to shielding and deshielding magnetic microenvironments, respectively, producing the unusual CISs observed for these protons in solution. Complementing the information obtained by NMR spectroscopy, the solid-phase structure also reveals a second stabilizing intermolecular hydrogen bond (O···H: 1.83 Å) between the carbamate carbonyl group of **SO1** and the amido-NH of **(*S*)-DNB-Leu**. This interaction and/or the proximity to the DNB-nitro function may account for the specific downfield shift of the H_{23} protons in the complex. The aromatic systems of **SO1** and **(*S*)-DNB-Leu** are found in a face-to-face orientation to one another with a mean interaromatic distance of about 3.5 Å, confirming complex stabilization by intermolecular $\pi-\pi$-stacking as predicted on the basis of NMR experiments. The existence and relative intensities of the intermolecular NOEs detected in solution are hence fully consistent with the solid-phase structure of the complex. The closest internuclear distance between the H_6 and H_{105} protons in **SO1** and **(*S*)-DNB-Leu** is about 3.57 Å, suggesting relatively weak dipolar interactions between these protons. The closest distances between H_{23} and H_{101}/H_{103} are significantly shorter (2.75 Å) which is in accordance to the build-up of more intensive NOEs. The relevance of the intermolecular NOEs detected between the aromatic H_{107} protons of **(*S*)-DNB-Leu** and the O_6-neopentyl H_6/H_7 and carbamate *tert*-butyl H_{23} of **SO1** is also confirmed, on the basis of the shortest internuclear distances (2.77 and 3.21 Å, respectively) found in the solid-phase structure of the complex.

Table 2. Averaged Potential Energies, Component Energies, and Solvation Energies for Water and Chloroform Simulations (kJ/mol) for **SO1·DNB-Leu** Interactions

	water			chloroform		
	SO·(*R*)-SA	SO·(*S*)-SA	Δ*E*	SO·(*R*)-SA	SO·(*S*)-SA	Δ*E*
total potential energy	−503.64	−509.30	−5.66	−461.44	−476.59	−15.15
stretch	154.52	154.46	−0.06	154.61	155.95	1.34
bend	208.01	208.01	0.00	209.65	209.39	−0.26
torsion	129.68	121.32	−8.36	131.50	123.19	−8.31
van der Waals	40.42	38.52	−1.90	51.52	43.11	−8.41
electrostatic	−840.49	−832.29	8.20	−900.65	−904.61	−3.96
solvation	−195.78	−199.32	−3.54	−108.07	−103.63	4.44

Energetics of Complexation With SO1. Computational chemistry allows one to extract information about intermolecular interactions not amenable to experimentation. However, before one can assess structural details about the competing diastereomeric complexes that form upon selector−selectand binding, the following prerequisites must be met: (1) The (*S*)-DNB-leucine analyte should be predicted to be longer retained on the column; that is, the complex with the (*S*)-selectand should have the lower energy. (2) The differential free energy of the competing diastereomeric complexes should compare well with the experimental separation factor, α, which, in this instance, is α = 32.0 with **SO1** at 25 °C, corresponding to a free energy difference of approximately 8.78 kJ/mol. (3) Crucial inter- and intramolecular nuclear Overhauser effects (NOE) seen experimentally must be reproduced computationally.

Because the chromatographic conditions used to evaluate the differential free energies of binding (80% methanol, 20% water) are different from those used to assess structural information of the complexes by NMR (methanol), two sets of computer experiments were carried out, both of which used continuum models to treat the solvent. The first experiment used a pure water continuum model to represent a high dielectric medium, and the second simulation used chloroform to represent a very low dielectric medium with the understanding that both the NMR and the chromatographic measurements had effective dielectrics somewhere between these extremes (the chromatography measurements being similar to the water simulations and the NMR measurements closer to the chloroform simulations). The total energies and solvation energies for these two sets of simulations are presented in Table 2. Because the total interaction energies consist of energies from bond stretching, angular deformation, and other contributing force field terms, we also present in Table 2 the time-averaged component energies for both diastereomeric complexes. The differences in energies between (*R*)- and (*S*)-complexes are given by Δ*E*, where a negative value means the (*S*)-complex is more stable.

The results from these nanosecond simulations indicate, for both high and low dielectric media, that the more retained enantiomer, corresponding to the more stable diastereomeric complex, has the (*S*)-stereochemistry; this is consonant with experiment. Next we find that the computed energy difference from the aqueous simulation (5.85 kJ/mol) underestimates slightly the experimental value (8.78 kJ/mol). However, this was anticipated because the simulation uses a pure water condition that should solvate excessively the ion pair as compared to the mixed water/methanol environment used experimentally. Contrary to this, but also expected, is that the energy difference for (*R*)- versus (*S*)-binding derived from the simulation in the low dielectric medium is overestimated (in this case by 6.27 kJ/mol). In this simulation, the ion pair is not

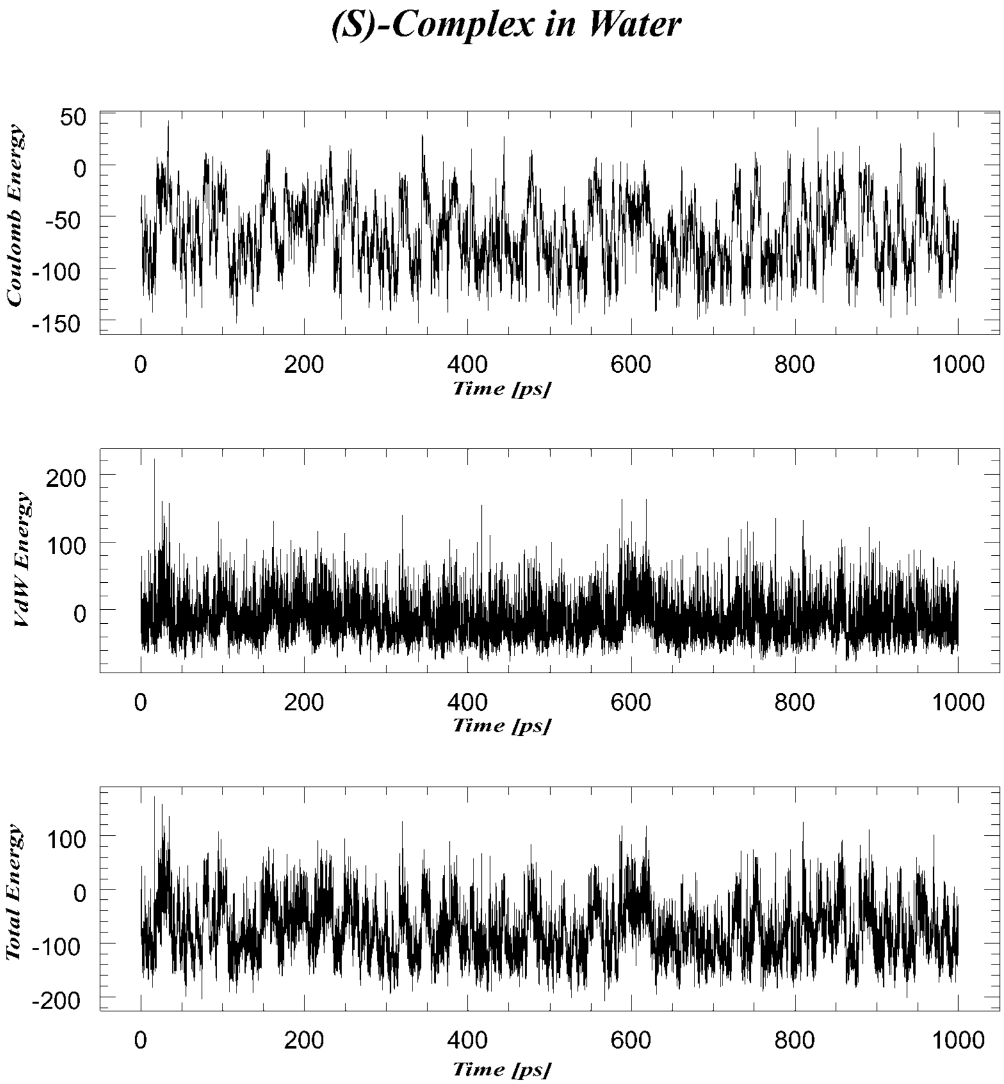

Figure 7. Trajectories of the intermolecular energies for the **(*S*)-DNB-Leu** binding to the protonated form of **SO1** over the 1 ns simulation time period in a polar (water) environment. Top: electrostatic (Coulomb) energy. Middle: van der Waals energy. Bottom: total energy.

quite solvated enough. The water simulation result, which should be compared with the chromatographic result, is in very good agreement with experiment (only 2.51 kJ/mol difference between experiment and theory). Hence, from these simulations we find that the computed retention order and differential free energies of binding are reproduced well by the AMBER* force field using a water continuum model. It will be shown below that whereas the high dielectric water system overly solvates the ion pair leading to a loosely associated complex, which in turn loses some chiral discriminatory power, low dielectric solvents allow for intimate ion pairing where chiral recognition is maximized.

We now consider the component energy terms in Table 2, reminding the reader that the lower numbers refer to the more stable system. In water, the stretching deformations are comparable for both complexes, but in the less polar chloroform, they favor the less tightly bound (*R*)-enantiomer (this means that less stretching deformations are involved in the less tightly held **SO1·(*R*)-DNB-Leu** complex than in the more tightly held **SO1·(*S*)-DNB-Leu** complex). The bending deformations for both diastereomeric complexes are the same in the highly polar water solvent but favor the more tightly bound (*S*)-enantiomer in the less polar chloroform solvent. In contrast to these energy differences, the torsional terms are large in both water and chloroform. The torsional energy presented here is a sum over all torsion angles. The torsion energy describes the deformation energy from ideal torsion angles (for all dihedral angles), and in these diastereomeric complexes, we find that a lot of torsional flexing (from ideality) exists throughout the simulation. Indeed, as will be shown later in this paper, the selector has undergone a substantial structural reorganization from its preferred shape in the free state so that suitable ion pairing with the selectand can occur. The work needed to preorganize the system for SO−SA binding (an intramolecular affair) is of course offset by the intermolecular stabilization that occurs upon SO−SA binding. These simulation results are in agreement with the ^{1}H NMR

Table 3. Intermolecular Energies (kJ/mol) of Competing Diastereomeric **SO1·DNB-Leu** Complexes in Water and Chloroform

	water			chloroform		
	SO·(*R*)-SA	SO·(*S*)-SA	Δ*E*	SO·(*R*)-SA	SO·(*S*)-SA	Δ*E*
total	−63.26	−81.25	−17.99	−55.77	−98.12	−42.35
van der Waals	−12.90	−14.15	−1.25	−1.25	−8.41	−7.16
electrostatic	−50.35	−67.10	−16.75	−54.52	−90.49	−35.97

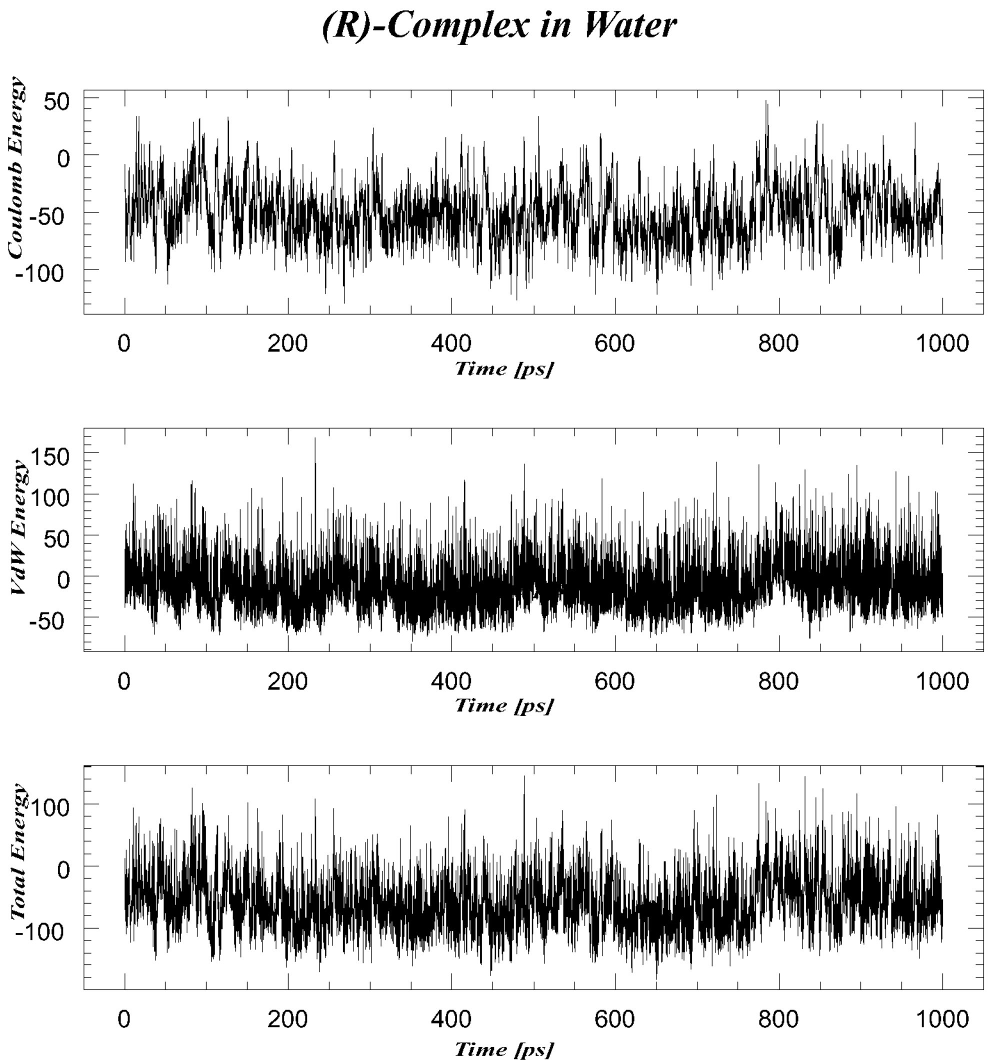

Figure 8. Trajectories of the intermolecular energies for the **(*R*)-DNB-Leu** binding to the protonated form of **SO1** over the 1 ns simulation time period in a polar (water) environment. Top: electrostatic (Coulomb) energy. Middle: van der Waals energy. Bottom: total energy.

results that indicate a partial or complete transition from a mixed closed-open conformation regime to the open conformation.

The aforementioned component energies are all considered to arise from "bonding" terms in the force field because atoms involved in those terms are connected to one another contiguously. Contrary to this, the remaining three component energies in Table 2 involve "nonbonded" interactions, that is, atom−atom interactions that are 1,3 or greater in nature. In both water and chloroform environments, the van der Waals terms (VDW) favor the more stable (*S*)-enantiomer, thus indicating that in the **SO1·(*S*)-DNB-Leu** complex there exists a better SO−SA fit than in the corresponding (*R*)-complex such that the van der Waals surface interactions are maximized. The electrostatic and solvation preferences change, however, depending upon the medium considered. In water, the electrostatic contributions favor the (*R*)-enantiomer, while in chloroform, they favor the (*S*)-enantiomer. The preference for electrostatic attraction of the (*R*)-enantiomer is counterintuitive, but, as we will point out below, the complex of the less tightly held (*R*)-enantiomer is far more flexible than is the complex of the (*S*)-enantiomer (especially in an aqueous medium). Under these conditions, we find that the three major stabilizing interactions found in the **SO1·(*S*)-DNB-Leu** complex (salt bridging, hydrogen bonding, and π-stacking) cannot exist *simultaneously* in the complex with the (*R*)-enantiomer, and, consequently, in the less structured complex the SA is pulled toward the SO in a way that maximizes the powerful electrostatic attractions. This electrostatic attraction for the less retained (*R*)-enantiomer takes place at the expense of other stabilizing intermolecular associations, however, which are retained in the (*S*)-complex. It is imperative to recall that the total potential energy being computed here is a sum of all energies averaged over the simulation time period. One should not be concerned that the less stable complex is favored electrostatically in this highly ionizing medium; this diastereomeric complex is ultimately disfavored as compared to that containing the (*S*)-enantiomer (as found experimentally) because of fewer other stabilizing terms.

We will return to the issue of diastereomeric complex flexibility and the impact this issue has on chiral recognition later in the paper. Moreover, it will be pointed out below that these energies refer to all of the atom−atom interactions in the complex; that is, the energies in Table 2 are a composite of both intra- and intermolecular energies combined. Below we will extract from these data only the intermolecular energies and discuss them separately with respect to chiral discrimination.

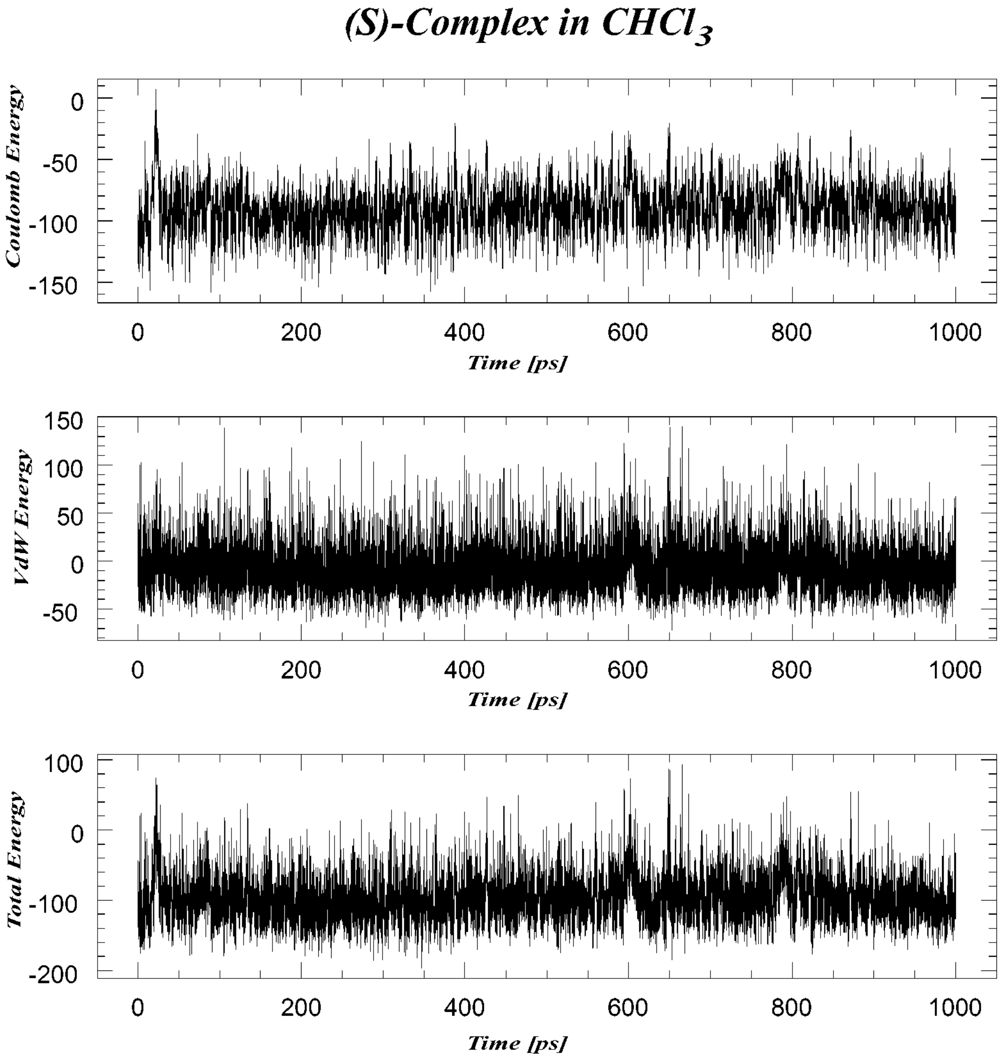

Figure 9. Trajectories of the intermolecular energies for the **(*S*)-DNB-Leu** binding to the protonated form of **SO1** over the 1 ns simulation time period in a nonpolar (chloroform) environment. Top: electrostatic (Coulomb) energy. Middle: van der Waals energy. Bottom: total energy.

Intermolecular Forces Leading to Chiral Discrimination. To obtain a more detailed picture of the stereodiscriminating process, the intermolecular forces responsible for chiral discrimination need to be extracted from the simulation data (the intermolecular terms that need to be considered are only the nonbonded VDW and Coulomb energies, hereafter called simply "nonbonded" energies). It is important to recognize that the nonbonded energies in Table 2 are not intermolecular energies alone. Instead, they are a composite of intra- *and* intermolecular nonbonded energies (in molecular mechanics force fields, the nonbonded interactions are computed pairwise additive meaning that all atoms experience all other nonbonded atoms, whether those other atoms are part of the same molecule or of a different molecule). We have written a program that extracts from these data only the intermolecular components.[37] Those values, averaged over the simulation time period, are presented in Table 3.

Several points of significance are derived from Table 3. First, under all conditions, both the van der Waals and the Coulomb interactions between the molecules are attractive (negative energies). Second, the dominant stabilizing force holding each complex together is from the electrostatic term. In this regard, we see that for the (*R*)-enantiomer in a water environment, 80% of the total intermolecular energy is attributable to Coulomb attractions, while for the more stable (*S*)-enantiomer, 83% is because of electrostatics; in a low polar medium, these contributions increase to 94% for the (*R*)-enantiomer and 95% for the (*S*)-enantiomer, respectively. Third, the most insightful aspect of these results concerning chiral recognition is the *differenc*e in energy between the **SO1·(*S*)-DNB-Leu** and the **SO1·(*R*)-DNB-Leu** diastereomeric complexes, denoted as ΔE in Table 3. This difference is a measure of chiral discrimination, and in this regard while we find that both the van der Waals and the Coulomb attractions between the molecules in the binary complex favor the longer retained (*S*)-enantiomer; the larger enantiodiscriminating force is attributed to the long-range electrostatic effects rather than to the short-range dispersion forces. These findings are in contradistinction to similar studies of cyclodextrins where the short-range forces dominate the chiral recognition process,[38,39] and this may be one reason the cinchona alkaloid-based SOs are far better chiral discriminators (for a

---

(37) Peterson, M. A. Understanding Enantiodifferentiation through Molecular Simulations. Ph.D. Thesis, Purdue University, 1996.

(38) Lipkowitz, K. B.; Pearl, G.; Coner, B.; Peterson, M. A. *J. Am. Chem. Soc.* **1997**, *119*, 600−610.

(39) Lipkowitz, K. B.; Stoehr, C. M. *Chirality* **1996**, *8*, 341−350.

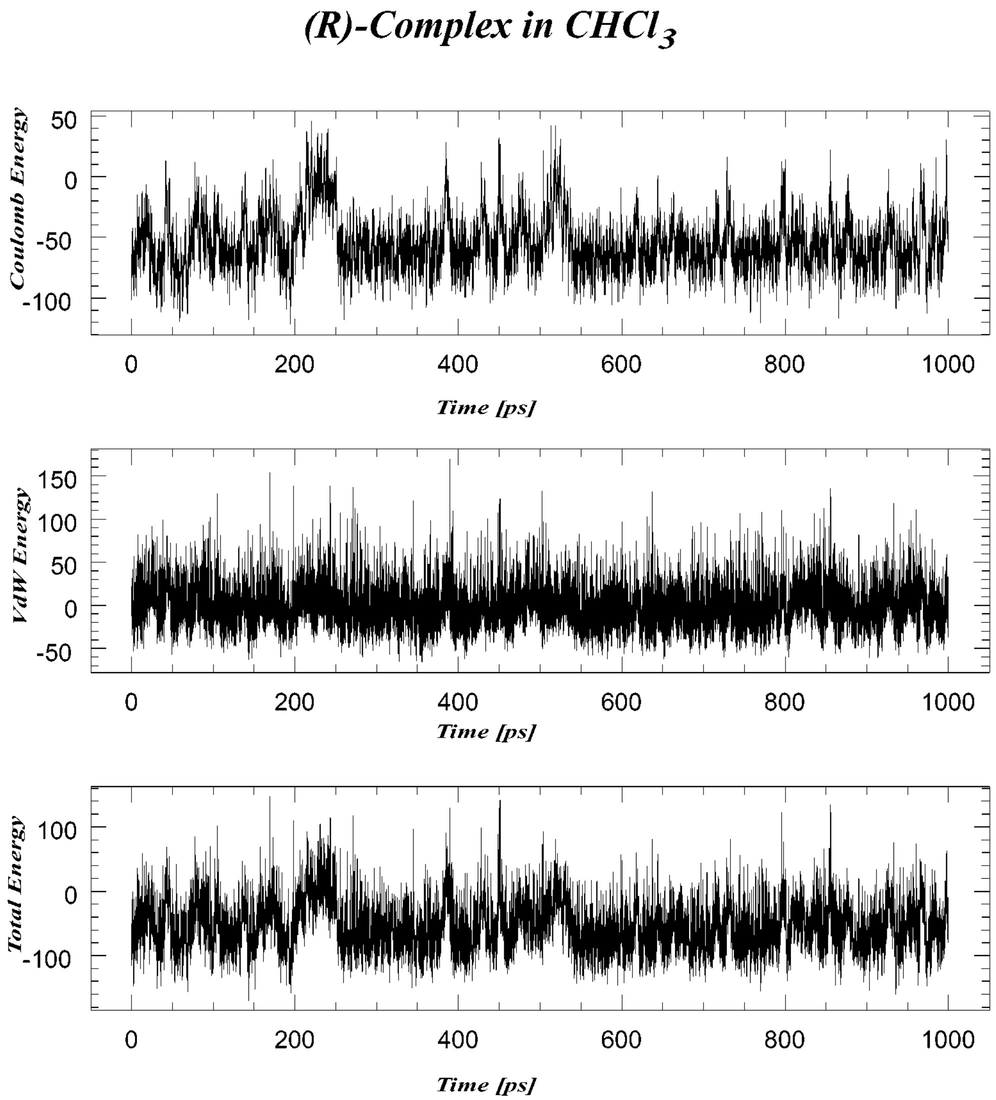

Figure 10. Trajectories of the intermolecular energies for the **(*R*)-DNB-Leu** binding to the protonated form of **SO1** over the 1 ns simulation time period in a nonpolar (chloroform) environment. Top: electrostatic (Coulomb) energy. Middle: van der Waals energy. Bottom: total energy. Note that for this less retained (*R*)-enantiomer there exist significant disruptions of the electrostatic attractions as compared to the more tightly held (*S*)-enantiomer in Figure 9.

limited class of compounds) than are the cyclodextrins. We also remind the reader to not think of this discriminating force as arising exclusively from the salt bridge formed between the carboxylate of the SA and the ammonium of the SO; even though those regions of the molecule are formally charged, all other atoms have partial atomic charges, and they too are contributing to the electrostatic energies being described here. In a forthcoming section, we will focus on which fragments of the SA are actually most responsible for chiral discrimination.

The intermolecular energies listed in Table 3 are average values; they do not indicate how those energies can fluctuate in time, nor do they describe the distribution of energies that occurred during the simulation time period. During the simulation, as the molecules are free to move about and collide with one another, both the inter- and intramolecular forces have changed. Below we provide two ways of visualizing these changes. The first, depicted in Figures 7 and 8, are plots of how the intermolecular energies between **SO1** and the **DNB-Leu** enantiomers change as a function of time (a trajectory) in a polar water medium. Similar plots for the chloroform simulations are given in Figures 9 and 10.

That there exist huge variations in intermolecular energy as the system evolves in time is evident from these trajectories. In particular, note that because of thermal collisions, the selectand moves and reorients itself with respect to the selector, albeit while remaining in a localized binding region around **SO1**. During this reorientation mode, both the electrostatic and the van der Waals energies are undergoing large fluctuations in magnitude (the sharp, noiselike spikes in the figures). Some differences in the intermolecular energy plots are discernible; in particular, we note that the electrostatic energies for the more tightly bound (*S*)-enantiomer in chloroform (Figure 9) are very uniform throughout the simulation time period, while the less retained enantiomer (Figure 10) contains points along the trajectory (e.g., 200−250 ps) where Coulomb attractions are disrupted. In water, we see far more disruptions of electrostatic attractions between **SO1** and the SAs than in the less polar solvent. The average energies from these trajectories were compiled in Table 3.

Another way of visualizing the intermolecular forces is to make a plot of the distribution of energies that were observed during the total simulation time period. These distributions are

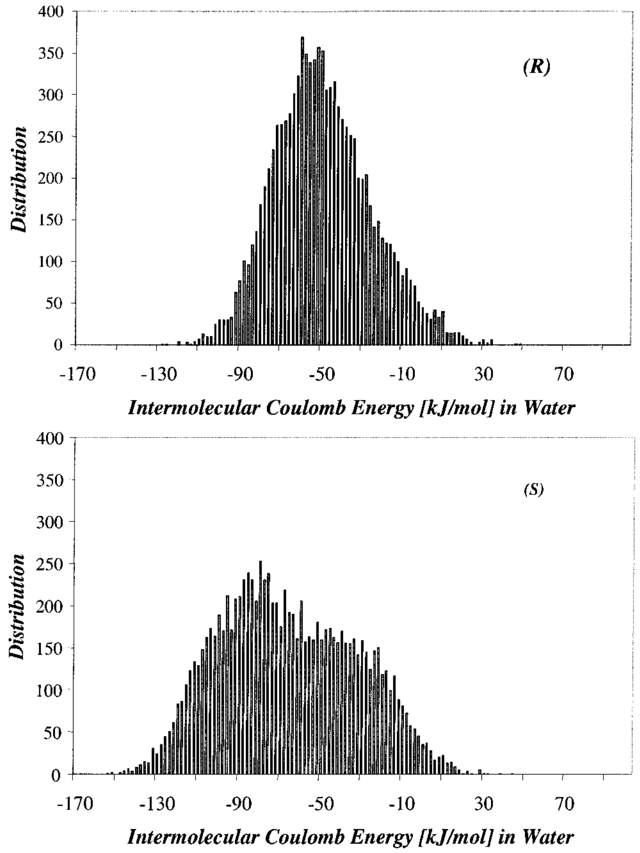

Figure 11. Distributions of electrostatic energies encountered during the simulation time period in water. The vertical axis is the number of occurrences, and the horizontal axis is the energy. Top: (*R*)-enantiomer. Bottom: (*S*)-enantiomer. Note that the more tightly bound (*S*)-enantiomer's distribution is shifted to lower energies than that for the (*R*)-enantiomer.

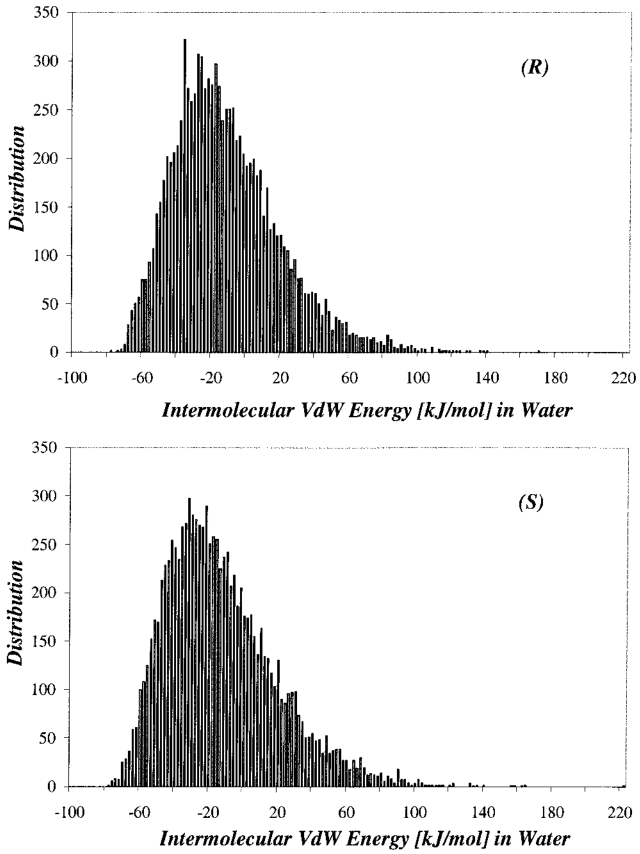

Figure 12. Distributions of van der Waals energies encountered during the simulation time period in water. The vertical axis is the number of occurrences, and the horizontal axis is the energy. Top: (*R*)-enantiomer. Bottom: (*S*)-enantiomer. Values to the right of zero are positive and destabilizing, while those to the left of zero are negative and stabilizing.

presented in Figures 11−16. In these figures, the energies, binned in units of 2 kJ/mol, are plotted as a function of the number of times a particular energy was encountered during the simulation time period. Figure 11 illustrates the distribution of the intermolecular electrostatic energies, while Figures 12 and 13 display the van der Waals and total energies, respectively, for the simulation in an aqueous environment. Figures 14−16 are the corresponding plots from the chloroform simulation. In the plots of the van der Waals energies, note that some values are negative (net attraction), while others are positive (net destabilization). In contrast, the Coulomb energies in Figures 11 and 14 are almost always negative and attractive.

The distribution of electrostatic interactions between selector and selectand in the chloroform solution is unimodal with a quasi-normal (Gaussian) distribution. The center of the distribution of the more tightly bound (*S*)-enantiomer is shifted to more negative (attractive) energies than for the (*R*)-enantiomer as expected. The distribution of electrostatic interactions in water is less normal than in a less polar solvent, especially for the (*S*)-enantiomer, which has its distribution heavily skewed toward the more negative direction. These plots and those for the VDW and the total intermolecular energies allow one to visualize better the intermolecular energies between **SO1** and SAs than from a trajectory plot or from a single number representing an average energy as compiled in Table 3. The plots further illustrate that the shapes of the distributions for (*R*)- and for (*S*)-enantiomers interacting with the selector are not much different from one another, indicating that only very subtle differences in intermolecular interactions are involved in the discrimination process.

Fragment Interactions. To better understand how **SO1** binds and discriminates between the **DNB-Leu** enantiomers, we consider now the interactions of molecular fragments that constitute the SO. We emphasize here that fragment energies are accessible by computations only and not by experiment. Partitioning the SO into fragments is a subjective and arbitrary decision. However, because there exist several characteristic, identifiable groups comprising this SO, we have divided the molecule into the four segments that are linked to C9 as illustrated in Figure 17.

In Table 4, we compile the intermolecular energies associated with each of these fragments interacting with the analyte molecule. In Table 4 we also dissect those total intermolecular energies into their van der Waals and electrostatic contributions (VDW/Coulomb energies, respectively, in Table 4). These energies are an average derived from all of the intermolecular associations that took place between **SO1** and the SAs during the simulation time period. Note that the sum of energies in Table 4 is slightly smaller than that in Table 3 because C9 was not included in the calculation of the fragment energies.

From this analysis, we find that the fragment most responsible for holding the complexes together is the carbamate group (see Table 4). The second most stabilizing interaction comes from the quinoline ring. This ring is seen in molecular graphics movies to form $\pi-\pi$-stacking associations with the DNB group of the analyte (see below). Significantly, the quinuclidine is

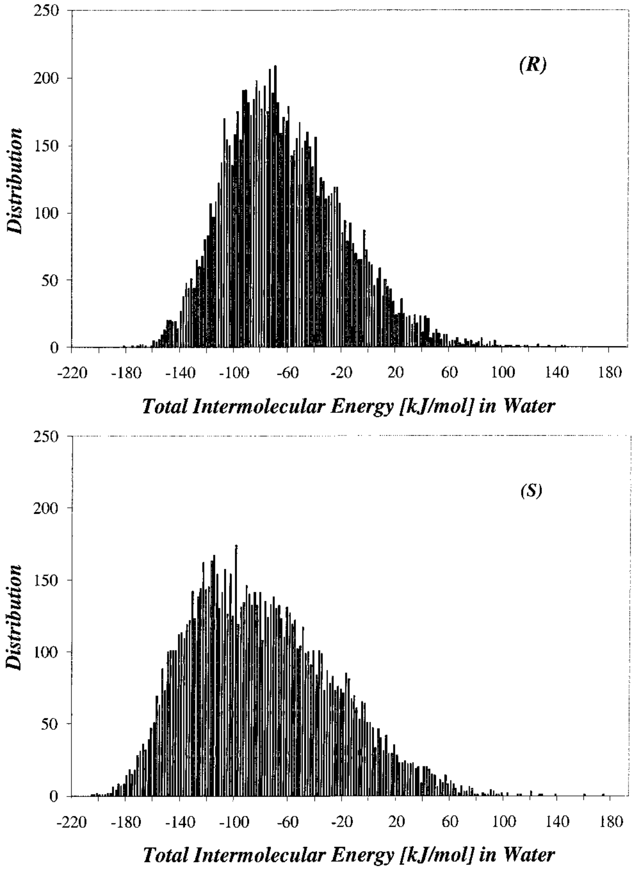

Figure 13. Distributions of the total intermolecular energies encountered during the simulation time period in water. The vertical axis is the number of occurrences, and the horizontal axis is the energy. Top: (*R*)-enantiomer. Bottom: (*S*)-enantiomer.

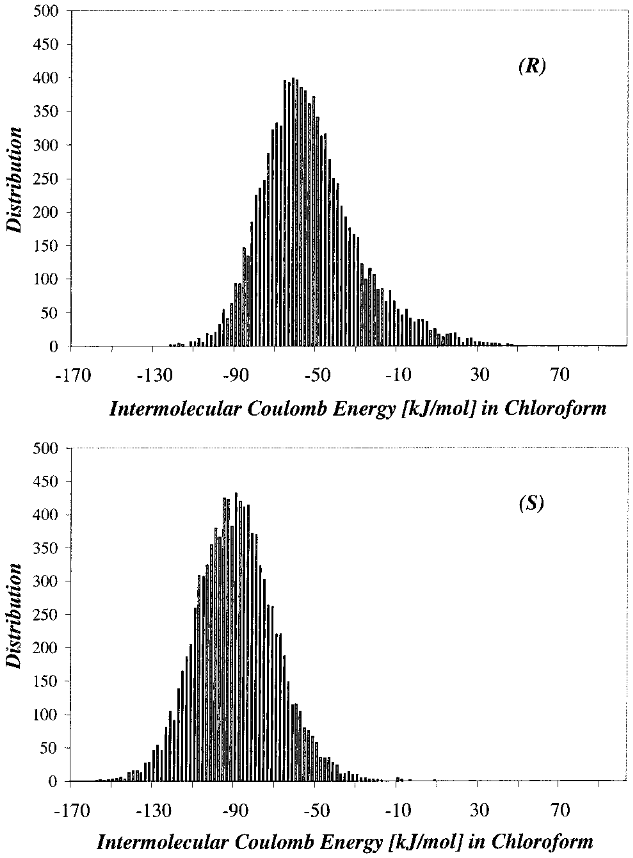

Figure 14. Distributions of electrostatic energies encountered during the simulation time period in chloroform. The vertical axis is the number of occurrences, and the horizontal axis is the energy. Top: (*R*)-enantiomer. Bottom: (*S*)-enantiomer. Note that the more tightly bound (*S*)-enantiomer's distribution is shifted to lower energies than that for the (*R*)-enantiomer.

relatively unimportant in either medium other than to provide a scaffold to which other fragments are connected. At first glance, this finding is both surprising and counterintuitive because this fragment bears the formal positive charge and forms the salt bridge between SO and SA. While this fragment does give rise to negative (attractive) electrostatic energies, those attractions are, however, offset by positive (repulsive) van der Waals interactions. In this context, we note that ion-pair formation exists in both diastereomeric complexes; therefore, this interaction contributes to the affinity but not much to the selectivity of bonding.

Before describing further these interactions, we ask how the time-averaged fragment energies in Table 4 compare with the energies of those same fragments in the static X-ray geometry. Using the solid-state atomic coordinates for our calculations, we find the intermolecular energy for the quinoline fragment of the selector interacting with the selectand to be −85.35 kJ/mol (−60.31 VDW and −25.05 Coulomb). The sign and magnitude of interaction for this fragment in the solid are thus comparable to the values for this fragment in solution as presented in Table 4. For the quinuclidine moiety, we find the interaction energy with the selectand is −21.86 kJ/mol (+14.31 VDW and −36.18 Coulomb). Hence, even in the solid state we find, as in Table 4, that there exists a subtle balance between attractive electrical interactions and repulsive steric interactions for this fragment. For the carbamate fragment in the solid-state geometry, the total interaction energy with the selectand is −104.07 kJ/mol; this is the fragment having the greatest interactions with the SA molecule. The large stabilization from this fragment arises from both favorable van der Waals energy (−14.50 kJ/mol) and favorable electrostatic contributions (−89.57 kJ/mol). The last fragment, the hydrogen on C9, is weakly repulsive by 1.65 kJ/mol. Hence, the physical picture derived from the solid-state geometry is that the carbamate fragment is most responsible for binding to the SA, the quinoline is second most responsible, and the quinuclidine is third most responsible for SA binding. This ordering of fragment contributions found in the solid is the same as the time-averaged values from the simulations, thus providing another internal consistency check on our simulation results. The intermolecular attraction of the carbamate moiety is dominated by electrostatic interactions. What is it about this fragment that makes it so stable? Using the X-ray geometry, we find that of the five most stabilizing intermolecular atom−atom interactions in the entire complex, the first four are associated with the carbamate. Figure 18 shows the key atom−atom pairs and their electrostatic attraction energies.

The second major point concerning these results involves the *difference* each fragment feels when associating with each **DNB-Leu** enantiomer. This difference is a measure of chiral discrimination, and in this regard the fragment showing the greatest difference between antipodes is the carbamate moiety. Hence, the fragment doing most of the work stabilizing the complexes (the carbamate) is also the fragment that is most enantiodifferentiating. This is an observation we also found in

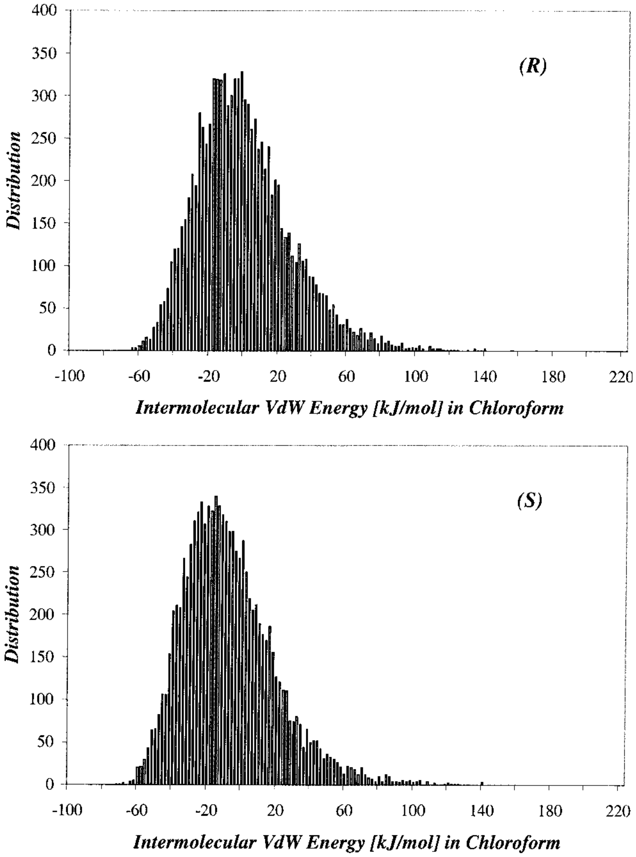

Figure 15. Distributions of van der Waals energies encountered during the simulation time period in chloroform. The vertical axis is the number of occurrences, and the horizontal axis is the energy. Top: (*R*)-enantiomer. Bottom: (*S*)-enantiomer. Values to the right of zero are positive and destabilizing, while those to the left of zero are negative and stabilizing.

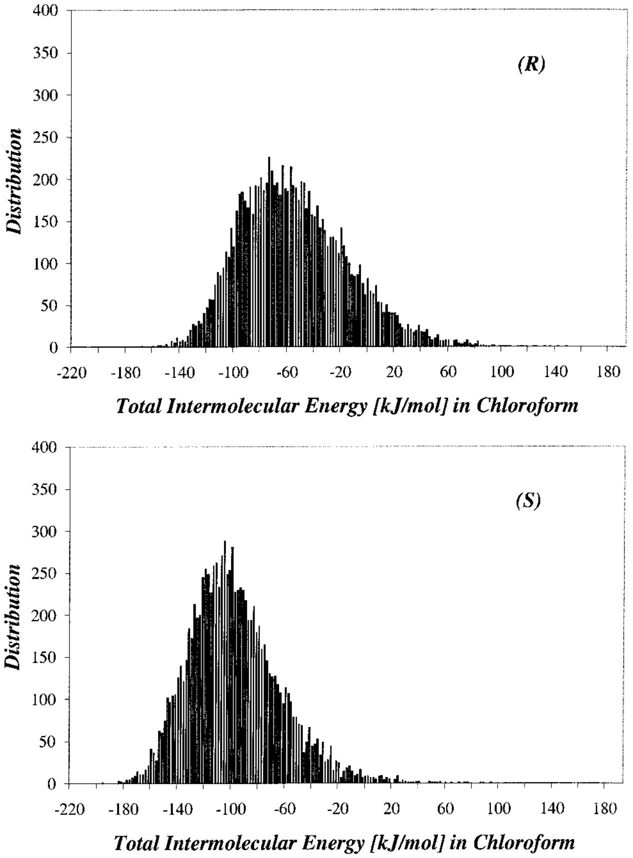

Figure 16. Distributions of the total intermolecular energies encountered during the simulation time period in chloroform. The vertical axis is the number of occurrences, and the horizontal axis is the energy. Top: (*R*)-enantiomer. Bottom: (*S*)-enantiomer.

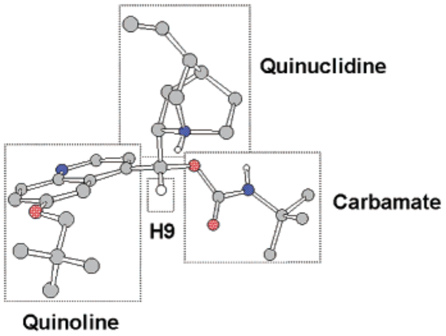

Figure 17. Partitioning of **SO1** into four molecular fragments. The atoms in each fragment are enclosed in boxes.

earlier studies of Pirkle-type SOs.[40] The quinoline moiety also displays significant chiral discrimination, but the other two groups do not. Finally, we see from Table 4 that for fragments that are most discriminating, the differential interaction energy (ΔE in the table) is larger for Coulomb contributions than it is for van der Waals contributions. Hence, these fragments discriminate primarily by long-range electrical effects rather than by short-range dispersion forces, a result that is in complete contrast to neutral cyclodextrin SOs where the dispersion forces were found to be most responsible for stereoselection. In summary then, we find the carbamate fragment to be the moiety most responsible for molecular association, and it is also the most enantiodiscriminating part of **SO1**.

Structural Features − Comparisons With NMR Data. Above we focused attention on the energetics of SO−SA binding; here we consider structural features of the diastereomeric complexes. In this section, we compare our results to NMR experiments described earlier, and we demonstrate that both inter- and intramolecular distances from the simulations are consonant with experimental NOEs. For these comparisons, we use only the data from the chloroform simulations. Below we shall make comparisons of our time-averaged conformations to the experimental X-ray-derived structure in the section called "Structural Features − Comparisons With X-ray Data". In Figure 6, we indicated which atoms give rise to NOEs. During the simulations, we collected 10 000 structures sampled uniformly in time along the trajectory. Using those structural snapshots, we then determined distributions of distances between selected atoms (and pseudo-atoms) for comparison with the NMR results. One way to present these data is by making a histogram showing the number of times a selected degree of freedom (a distance in this instance) has visited a particular range of interest. As an example of this, consider Figure 19.

In Figure 19, we show the distances between two dummy atoms that have been placed at aromatic ring centroids (one dummy atom is on the DNB ring of the selectand, and one dummy atom is on the quinoline's aromatic ring). A histogram plot of the distance between these centroids allows us to visualize quickly the average distribution of inter-ring distances, which in this case reflect $\pi-\pi$-stacking interactions. While many

---

[40] Lipkowitz, K. B.; Baker, B. *Anal. Chem.* **1990**, *62*, 770−774.

Table 4. Total Intermolecular Energies (kJ/mol) and VDW/Coulomb Component Intermolecular Energies (kJ/mol) for Fragments of **SO1** in the Diastereomeric **SO1·DNB-Leu** Complexes

	water			chloroform		
	SO·(*R*)-SA	SO·(*S*)-SA	Δ*E*	SO·(*R*)-SA	SO·(*S*)-SA	Δ*E*
Total Intermolecular Energies						
quinoline	−61.34	−70.93	−9.59	−56.72	−74.26	−17.54
quinuclidine	7.43	8.29	0.86	4.63	−1.09	−5.72
carbamate	−64.15	−80.03	−15.88	−64.92	−96.65	−31.73
hydrogen	0.81	1.39	0.59	1.82	3.23	1.41
VDW/Coulomb Component Intermolecular Energies						
quinoline	−38.4/−22.9	−42.3/−28.6	−3.9/−5.7	−40.1/−16.7	−48.1/−26.2	−8.1/−9.5
quinuclidine	38.8/−31.4	40.9/−32.6	2.0/−1.2	51.3/−46.7	51.7/−52.8	−0.4/−6.1
carbamate	−12.2/−52.0	−12.0/−68.1	0.2/−16.1	−12.1/−52.8	−12.6/−84.1	−0.5/−31.3
hydrogen	0.8/0.0	1.39/0.0	0.59/0.0	1.82/0.0	3.23/0.0	1.41/0.0

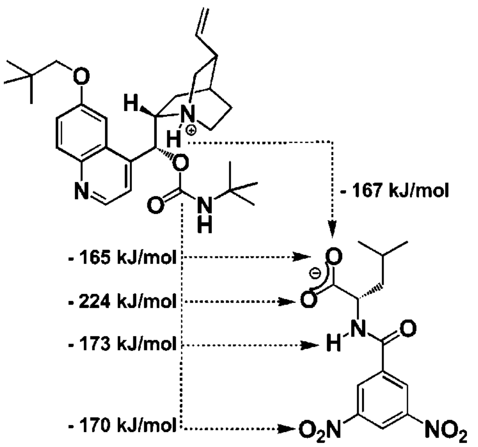

Figure 18. Diagram indicating which atom pairs in the **SO1·(*S*)-DNB-Leu** complex are most attractive electrostatically. Energies were computed with the AMBER* force field using the X-ray geometry and AMBER* assigned charges. It is to be noted that four of the five most stabilizing interactions are between the SA and the carbamate moiety of **SO1**.

such histograms were generated, we show only this one because a substantial difference between the plots exists. Most noticeable is that the complex containing the more strongly bound (*S*)-enantiomer is unimodal, while that with the (*R*)-enantiomer appears somewhat bimodal (a consequence of the system visiting more than one energy minimum on the diastereomer's potential energy surface). Moreover, we note that even in the unimodal distribution the distances are not symmetric, and the distribution is heavily skewed. Accordingly, presenting only the mean value of such distances can be misleading. The distributions in Figure 19 do not conform to a simple mathematical expression and are presented in histogram form for convenience only. Moments of distributions, however, provide a general basis for characterizing and comparing distributions. Although a distribution is characterized fully once all of its moments are known, many distributions can be described well by the first four moments.[41] The first central moment, μ_1, is always zero. The second moment, μ_2, is the variance, and the square root of the variance is the standard deviation. Hence, the second moment is related to the width of the distribution which in turn can provide insights about molecular rigidity/flexibility (the more rigid systems will have narrower distributions). The third moment about the mean, μ_3, is called the skewness of a distribution. For a normal distribution, that is, one that is perfectly symmetric, μ_3 is zero. If the distribution is skewed to the left, that is, it has a left tail, $\mu_3 < 0$, and if skewed right, $\mu_3 > 0$. Hence, the third moment is related to the asymmetry of the distribution. The fourth moment, μ_4, is called kurtosis. This measure is related to the peakedness or sharpness of the distribution as well as modality of distributions. A compilation of key atom−atom distances is provided in Table 5. We present in this table the mean value, the standard deviation, the skewness, and kurtosis for each distance considered.

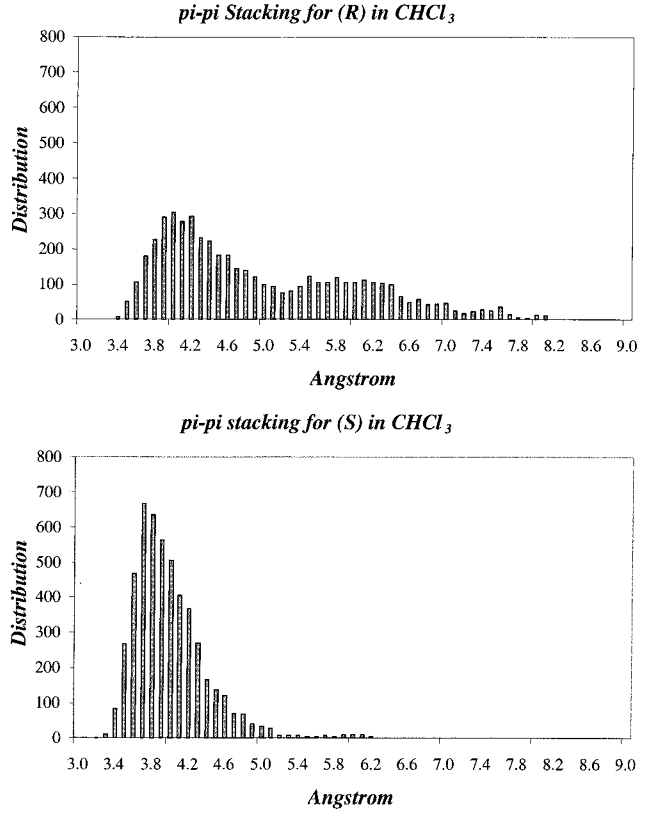

Figure 19. Histogram plots of intermolecular distances between dummy atoms placed at ring centroids of the neopentoxy-containing receptor **SO1** and the **DNB-Leu** enantiomers. Top: (*R*)-enantiomer. Bottom: (*S*)-enantiomer. The distance between centroids is related to $\pi-\pi$-stacking distances in the competing binary, diastereomeric complexes. Clearly evident is the bimodal distribution of distances for the less tightly bound enantiomer indicating visits to other minima on the potential energy surface of the diastereomeric complex that are absent when the more tightly held (*S*)-enantiomer binds.

One of the crucial intermolecular NOEs observed experimentally is between H_{105}, a methine proton connected to the stereogenic center of the selectand, with the methylene protons H_{6a} and H_{6b} on the selector's neopentoxy group. This NOE exists

---

(41) Lipkowitz, K. B.; Peterson, M. A. *J. Comput. Chem.* **1995**, *16*, 285−295.

Table 5. Distances (in Å) and Statistics of Distributions for Selected Atom−Atom Pairs (see Figure 2 for Atom Numbering) in the Diastereomeric Complexes of **SO1·DNB-Leu**

atom pair	mean (*R*)/(*S*)	std dev (*R*)/(*S*)	skewness (*R*)/(*S*)	kurtosis (*R*)/(*S*)
		Intermolecular		
$H_{105}-H_{6a}$	5.13/2.98	0.52/0.42	0.03/0.41	−1.47/0.17
$H_{105}-H_{6b}$	6.08/4.18	0.46/0.46	0.70/0.15	−0.15/0.94
centroids	4.23/3.95	0.33/0.41	−0.26/1.65	−0.40/4.54
		Intramolecular		
H_1-H_{11}	2.71/2.79	0.23/0.26	0.06/0.18	−0.16/0.02
H_5-H_8	2.37/2.38	0.13/0.19	−0.03/0.61	−0.60/0.51
H_5-H_9	2.20/2.17	0.11/0.11	0.37/0.46	−0.36/0.54

experimentally in the binary complex containing the (*S*)-SA, but not for (*R*)-SA. In Table 5, the mean distances between the methine and the two methylene protons are 2.98 and 4.18 Å for the (*S*)-enantiomer, placing these nuclei well within the range of an NOE, while those for the (*R*)-enantiomer are 5.13 and 6.08 Å, placing them outside the range of an observable NOE. These computed distances are actually on the low side as compared to experimental distances because the simulations were done at an effective dielectric of 4.7, while the NMR measurements were done in methanol which has a dielectric constant of 32.6. In water, those distances are computed to be even further apart (data not given in Table 5). The variance is greater for the less tightly bound (*R*)-enantiomer, and the kurtosis is leptokurtic (negative values indicating a slight bimodal distribution) for the (*R*)-enantiomer. In contrast, the (*S*)-enantiomer shows a unimodal distribution as reflected in a positive fourth moment.

These statistical measures indicate that the (*S*)-enantiomer retains its bound-state shape throughout the simulation time period in a low dielectric medium, but the (*R*)-complex does not; instead, the (*R*)-enantiomer undergoes several conformational changes including DNB ring flipping (stacking−unstacking−restacking) giving rise to a looser complex that has no observable intermolecular NOE. This behavior is nicely reflected by the ^{1}H NMR results: the existence of several intermolecular NOEs and characteristic complexation-induced shifts implicate that the (*S*)-complex is stable and sustains the SO−SA geometry on the NMR time scale, while the (*R*)-complex must be much more flexible, as intermolecular NOEs and CISs are not observed. The intramolecular NOEs observed experimentally include quinoline ring proton H_1 with the endo proton H_{11} of the quinuclidine ring and the quinoline ring proton H_5 with neighboring protons H_8 and H_9. These intramolecular NOEs are consistent with the anti-open conformation of the quinine-based **SO1** molecule as described earlier. The distances found in our simulations are in full accord with this geometry when either (*R*)- or (*S*)-SA is bound. More specifically, we find that the mean distance between H_1 and H_{11} is 2.79 Å in the (*S*)-complex and 2.72 Å in the (*R*)-complex, the mean distance between H_5 and H_8 is about 2.38 Å when either (*R*)- or (*S*)-SA binds, and the mean distance between H_5 and H_9 is 2.17 Å when the (*S*)-enantiomer is bound and 2.20 Å when the (*R*)-enantiomer is bound.

Hence, all crucial experimental intramolecular NOEs are fully accounted for in our simulations. We then conclude that the anti-open conformation of the SO is the only one detectable for the more stable complex. For the weaker complex, anti-open is still the preferred shape, but there exists also the presence of the closed conformer. Overall, we stress here that the above-described findings are in excellent agreement with the experimental data in respect to both NMR and X-ray structure-based evidence. Finally, we point out that the distances between the aromatic rings are indicators of whether $\pi-\pi$-stacking exists. To monitor this, we computed two centroids; one of them is on the DNB group, and the other is on the quinoline ring (this centroid lies along the bond that fuses the two rings together). The distance between these centroids was plotted in Figure 19 above. The mean distance between centroids when the (*S*)-enantiomer binds is 3.95 Å, and the mean distance between centroids in the less stable **SO1·(*R*)-DNB-Leu** complex is 4.23 Å. While the skewness for the (*S*)-enantiomer is positive, that for the (*R*)-enantiomer is negative. More significantly, though, is that the kurtosis for the (*S*)-enantiomer is positive (unimodal), while that for the (*R*)-enantiomer is negative (bimodal). These values reflect the dynamical nature of the two different complexes; in one case ((*S*)-enantiomer), the system rolls over a low energy basin of the potential energy surface, but in the other case ((*R*)-enantiomer), the system hops from basin to basin, with disruption of $\pi-\pi$-stacking.

Structural Features − Comparisons With X-ray Data. We describe here the time-averaged structural features of the more stable binary complex as compared to the geometry in the solid state derived from X-ray crystallography (vide supra). Our focus here is on the shape of **SO1** as it experiences interactions with **(*S*)-DNB-Leu**. During the simulation, we assessed the distribution of critical dihedral angles for purposes of describing mean values, the statistical evaluation of their distributions, and also their dynamical properties. The key angles monitored and their values are compiled in Table 6.

Before discussion of these results, we point out that the X-ray coordinates are close to, but not at, a minimum energy structure

Table 6. Important Dihedral Angles (in deg) of the X-ray Structure (bold), Mean Values, and Moments of Distributions from MD Simulations for **(*R*)-** and **(*S*)-DNB-Leu** Enantiomers Bound to **SO1**

dihedral	mean (*R*)/(*S*)**[X-ray]**	std dev (*R*)/(*S*)	skewness (*R*)/(*S*)	kurtosis (*R*)/(*S*)
$O_{25}-C_{25}-O_9-C_9$	14/8 **[−3.9]**	29.46/14.36	1.59/−0.24	3.36/0.09
$C_{25}-O_9-C_9-H_9$	40/32 **[9.7]**	11.71/11.69	−0.33/−0.08	0.55/0.09
$N_1-C_8-C_9-O_9$	−65/−67 **[−79.1]**	8.56/7.35	0.21/0.10	0.42/0.22
$C_{27}-C_{26}-C_9-O_9$	155/158 **[163.9]**	12.56/10.92	−14.78/−17.56	388.0/537.8
$C_{28}-C_{29}-O_6-C_{30}$	24/5 **[−10.5]**	49.90/14.32	0.36/−0.03	5.06/0.38
$C_{29}-O_6-C_{30}-H_{31}$	−192/−187 **[−167.3]**	22.04/14.84	0.89/−1.06	3.38/−3.90
$C_{109}-C_{110}-C_{112}-C_{111}$	−79/−144 **[−158.3]**	71.01/48.40	1.51/5.98	2.95/36.15
$C_{112}-N_{113}-C_{114}-H_{105}$	37/−18 **[19.8]**	18.09/12.26	−0.36/5.98	−0.38/0.07
$N_{115}-C_{114}-C_{115}-C_{116}$	33/−63 **[−62.2]**	146.62/75.39	−0.54/1.98	−1.48/4.72
$C_{102}-C_{116}-C_{115}-C_{114}$	10/33 **[54.2]**	51.01/40.50	−0.30/−1.53	−1.61/0.93

on the diastereomer's AMBER* potential energy surface. When all heavy atoms of the X-ray structure are compared to all heavy atoms of the energy minimized structure, a root-mean-squared deviation (rmsd) of 0.65 Å is obtained (i.e., the energy minimized geometry is very similar to the X-ray geometry). A similar comparison of the time-averaged structure derived from our simulations as compared to the solid-state X-ray geometry has a rmsd of 0.86 Å, thus illustrating that the more stable diastereomeric complex retains well its solid-state geometry throughout the simulation. For the sake of completeness, the X-ray dihedral angles are also included in Table 6.

The results in Table 6 show that the more stable diastereomeric complex (containing **(*S*)-DNB-Leu**) has a geometry that is similar to the complex in the solid state, while the less stable complex is less well bound and thus has a less well-defined shape.

Conclusions

Chromatographic experiments carried out with an immobilized version of **SO1** have established highly enantioselective binding properties for **DNB-Leu**, the (*S*)-enantiomer being more strongly bound. ^{1}H NMR experiments performed in methanol-d_4 with the diastereomeric **SO1·DNB-Leu** complexes confirmed that this receptor and the analytes associate with 1:1 stoichiometry as a consequence of ion-pair formation. Analysis of inter-ring NOEs provided evidence that enantioselective binding induces significant conformational reorganization of the receptor. Specifically, **SO1** experiences a transition from a closed/open to the anti-open conformational status on binding **(*S*)-DNB-Leu**; this effect was less prominent with the (*R*)-enantiomer, indicating different interaction modes with the receptor. The analysis of complexation-induced shifts revealed significant effects for the more stable **SO1·(*S*)-DNB-Leu** complex and provided evidence for the crucial role of ion-pairing, $\pi-\pi$-stacking interaction, and hydrogen bonding as simultaneously acting intermolecular forces contributing to complex stabilization. By contrast, for the less stable diastereomeric complex **SO1·(*R*)-DNB-Leu**, changes in chemical shifts were less pronounced and unspecific. Here, only shifts indicating complex stabilization by ion pairing were observed. In particular, no indication for stabilizing intermolecular $\pi-\pi$-interaction could be found. Intermolecular NOEs were only observable for **SO1·(*S*)-DNB-Leu**, but not the less stable diastereomeric complex. Pooling various types of information from the NMR studies allowed us to advance a model of the time-averaged geometry of the more stable **SO1·(*S*)-DNB-Leu** complex in solution. In this complex, **SO1** provides a well-defined binding domain for **(*S*)-DNB-Leu**, being located between the O_6- and O_9-substituents attached to the cinchona skeleton. In this binding pocket, the analyte is recognized and bound by multiple simultaneously acting intermolecular interactions, including ion-pairing, hydrogen bonding, and highly effective $\pi-\pi$-stacking interactions, leading to an exceptionally high degree of enantioselective recognition. An X-ray crystal structure of **SO1·(*S*)-DNB-Leu** is in excellent agreement with the interaction model established for the solution phase by NMR spectroscopy. All crucial structural features predicted by NMR spectroscopy for **SO1** are also found in the solid phase, in particular, the anti-open conformation and the relative orientation of the interaction site-forming substituents. Moreover, the solid-phase structure of the complex corroborates the cooperative set of intermolecular interactions between **SO1** and **(*S*)-DNB-Leu** postulated on the basis of the NMR results.

Stochastic dynamics simulations of the enantioselective complex formation of **SO1** with the enantiomers of **DNB-Leu** have been carried out successfully. Both the retention order and the differential free energy of binding found experimentally have been calculated with a high degree of precision. Moreover, crucial inter- and intramolecular NOEs observed experimentally are reproduced computationally. Detailed structural assessments of simulation results with NMR results were made as well as evaluations of structural features of SO−SA complex geometries as compared with X-ray results. In all cases, the "anti-open" conformation of the SO was found. On the basis of these simulations, we were able to dissect the total energy of the system into force field component energies. It was found that in water the largest difference between the free energies of these complexes originated from the Coulomb contributions which favor the (*R*)-enantiomer and from torsional contributions that favor the (*S*)-enantiomer. In nonpolar solvents, both of those contributing terms favor the more retained (*S*)-enantiomer. Also, in the less polar solvent, there exist maximum van der Waals associations favoring the (*S*)-enantiomer. The issue of binding site was not explicitly addressed computationally, but we found that both SAs are bound via salt bridges, hydrogen bonding, and π-stacking to **SO1** and are spatially restricted to a very constrained region around the selector with the (*S*)-enantiomer being nearer to **SO1** than the (*R*)-enantiomer. Although confined spatially, both SAs undergo wide-amplitude rocking motions and form stacked $\pi-\pi$-associations with the SO, albeit with different frequencies; the more tightly bound enantiomer maintains this association throughout the simulation time period, while the less tightly bound isomer dissociates and then reforms the π-stacking.

The intermolecular energies between **SO1** and the **DNB-Leu** enantiomers were extracted from the total energies of the diastereomeric complexes. It was shown that the dominant intermolecular stabilization arises from electrostatic attractions and that the enantiodifferentiating intermolecular energy arises mainly from the long-range electrical interactions rather than from the short-range dispersion forces as found in cyclodextrin selectors. It is speculated that perhaps this is one reason our cinchona alkaloid-based **SO1** is far more enantiodiscriminating than are the cyclodextrins (at least for a limited number of types of compounds that we have studied to date). **SO1** was divided into four fragments, and an energy analysis of those fragments interacting with the analytes was carried out. We found that the fragment most responsible for holding the complex together is the carbamate group (four of the five most stabilizing interactions between selector and selectand are associated with that fragment) and the second most stabilization comes from the quinoline ring. The quinoline acts as a π-base that forms stacking associations with the π-acidic DNB group of the SAs. Moments of distributions of important atom−atom pairs provided insights about the relative goodness of fit between the molecules comprising the diastereomeric complexes and allowed us to provide some quantitative measure of each diastereomer's rigidity in different solvent environments. Clear differences in π-stacking were observed in the competing diastereomeric complexes, and it was pointed out that while three simultaneous intermolecular interactions (salt bridging, hydrogen bonding, and

π-stacking) can be achieved for the more stable SO−SA complex, this is not possible for the less stable complex.

Experimental Section

General. All reactions were carried out under strictly anhydrous, air-free conditions. All solvents were dried and distilled by standard procedures. For characterization of products, the ^{1}H spectra were acquired on a Bruker DRX 400 MHz spectrometer. The ^{1}H chemical shifts are given in parts per million (δ) with respect to TMS as a standard. FTIR spectra were recorded on a Perkin-Elmer Spectrum 2000 spectrometer, and optical rotations were recorded on a Perkin-Elmer 341 polarimeter at 25 °C.

Materials. Cupreine was prepared from quinine using a protocol reported for the transformation of quinidine to cupreinidine.[42] (*R*)-DNB-Leu was synthesized from (*R*)-leucine and 3,5-dinitrobenzoyl chloride according to the literature.[16] All other chemicals and solvents were purchased from Aldrich Chemical Corp.

6-Neopentoxy-cinchonidine. A 100 mL flask was charged with cupreine (5.00 g, 16.1 mmol) and 50 mL of *N*-methylpyrrolidone to yield a clear, slightly yellowish solution. To this were added finely powdered cesium carbonate (7.50 g, 23 mmol, dried at 120 °C in vacuo prior to use) and neopentylbromide (3.0 mL, 3.62 g, 24 mmol). The mixture was heated at 130 °C with stirring for 24 h. The solvent was removed in high vacuo (0.07 mbar, 80−100 °C bath temperature). The resultant black paste was distributed between chloroform (200 mL) and water (200 mL). The organic phase was washed with more water (2 × 150 mL), dried with $MgSO_4$, and concentrated under reduced pressure. The dark oily residue was subjected to flash chromatography (100 g of silica, gradient elution with methanol in chloroform, 0−10%) to yield 4.76 g (78%, 12.5 mmol) of a solid. A crystalline, colorless solid was obtained after recrystallization from ethyl acetate/hexanes: mp 158−160 °C. $[\alpha]_D = -162.7°$ ($c = 1.25$, methanol). ^{1}H NMR ($CDCl_3$): δ 8.71 (d, 1H), 8.02 (d, 1H), 7.51 (d, 1H), 7.38 (dd, 1H), 7.26 (s, 1H), 5.79 (m, 1H), 7.52 (d, 1H), 4.99 (d, 1H), 4.75 (d, 1H), 3.71 (m, 3H), 3.51 (m, 1H), 3.20 (m, 1H), 3.12 (dd, 1H), 2.74 (m, 1H), 2.69 (m, 1H), 2.28 (m 1H), 1.85 (m, 1H), 1.76 (overlapped m's, 3H), 1.63 (m, 1H), 1.51 (m, 1H), 1.09 ppm (s, 9H). IR (KBr): 3165, 1621, 1590, 1510, 1459, 1402, 1364, 1241, 1228 cm^{-1}. Anal. Calcd for $C_{24}H_{32}N_2O_2$: C, 75.75; H, 8.48; N, 7.36. Found: C, 75.70; H, 8.50; N, 7.32.

9-(*tert*-Butylcarbamoyl)-6-neopentoxy-cinchonidine (SO1). 6-Neopentoxy-cinchonidine (2.28 g, 6.0 mmol) was dissolved in 20 mL of dry toluene. After addition of *tert*-butylisocyanate (0.70 g, 7.0 mmol) and a catalytic amount of dibutyltindidodecanate (50 μL, 85 μmol), the clear solution was refluxed for 25 h. The volatiles were removed in vacuo, and the residue was subjected to flash chromatography (30 g of silica, chloroform/methanol = 20/1) to give 2.76 g (96%, 5.76 mmol) of **SO1**. A crystalline colorless solid was obtained after recrystallization from ethyl acetate/hexanes: mp 148−150 °C. $[\alpha]_D = -15.4$ ($c = 1.0$, methanol). ^{1}H NMR ($CDCl_3$): δ 8.72 (d, 1H), 8.03 (d, 1H), 7.47 (s, 1H), 7.40 (dd, 1H), 7.27 (d, 1H), 6.48 (d, 1H), 6.87 (m, 1H), 5.05 (d, 1H), 5.00 (d, 1H), 4.79 (s, 1H), 3.76 (q, 3H), 3.33 (m, 1H), 3.15 (m, 1H), 3.08 (m, 1H), 2.70 (m, 1H), 2.66 (m, 1H), 1.85 (m, 1H), 1.76 (overlapped m's, 2H), 1.61 (m, 1H), 1.54 (m, 1H), 1.30 (s, 9H), 1.09 (s, 9H). IR (KBr): 3271, 2953, 2868, 1720, 619, 1590, 1510, 1455, 1396, 1364, 1267, 1094 cm^{-1}. Anal. Calcd for $C_{29}H_{41}N_3O_3$: C, 72.62; H, 8.62; N, 8.76. Found: C, 72.64; H, 8.65; N, 8.74.

Preparation of CSP1. CSP1 was prepared by immobilization of **SO1** onto mercaptopropyl-modified spherical silica following a well-established procedure.[6] The level of selector loading (0.24 mmol/g) was established by CHN analysis on the basis of the nitrogen content of the modified silica as basis for the calculation. For liquid chromatographic evaluation, **CSP1** was packed into stainless steel columns (150 × 4 mm i.d.) employing standard slurry packing procedures.

Determination of the Chromatographic Enantioseparation Factors (α) by HPLC. The enantioseparation factor (α) was determined as a ratio of the retention factors of the individual enantiomers of **DNB-Leu** ($\alpha = k_S/k_R$; $k_S > k_R$) observed with **CSP1** in HPLC experiments. The experiments were carried out under the following chromatographic conditions: column dimensions, 150 × 4 mm i.d.; mobile phase, 0.1 M aqueous ammonium acetate/methanol = 20/80; $pH_a = 6.0$, adjusted with acetic acid; flow rate, 1 mL/min; UV-detection, 254 nm; column temperature, 25 °C; injected sample amount, 20 μg (*R,S*)-dinitrobenzoyl leucine; thiourea was used as a void volume marker. The chromatographic runs were performed in triplicate, and standard deviations for the enantioseparation factors were <0.1. The enantioselectivity for **DNB-Leu** on **CSP1** was $\alpha = 32.6$ ($k_R = 6.38$, $k_S = 207.90$).

NMR Experiments. The monohydrochloride of **SO1** was prepared by addition of an equivalent amount of methanolic hydrogen chloride, evaporation of the solvent, and drying in a vacuum. In similar fashion, the sodium salt of **DNB-Leu** was obtained by addition of an equivalent amount of methanolic sodium methoxide solution, evaporation, and drying in a vacuum. The 1:1 complexes of **SO1** and the individual enantiomers of **DNB-Leu** were prepared by dissolving stoichiometric amounts of the corresponding components. ^{1}H NMR experiments were carried out with a Bruker AMX 500 and a Varian VXR 5 spectrometer operating at 500 MHz at a temperature of 298 ± 0.1 K. All measurements were performed in methanol-d_4. Degassing was achieved by passing a stream of argon through the samples for 5 min. The complexation stoichiometry for **SO1·(*S*)-DNB-Leu** and **SO1·(*R*)-DNB-Leu** was established by the continuous variation protocol[27] using the chemical-induced shifts of H_9 as diagnostic resonances. Signal assignment of the ^{1}H NMR spectra of **SO1**, **SO1·HCl**, **DNB-Leu**, the sodium salt of DNB-Leu, and the diastereomeric complexes **SO1·(*S*)-DNB-Leu** and **SO1·(*R*)-DNB-Leu** was assisted by ^{1}H−^{1}H correlation (COSY), nuclear Overhauser enhancement (NOESY), and heteronuclear multiple quantum coherence (HMQC) spectroscopy. Typical NOESY spectra were obtained for a spectral width of 4780 × 4780 Hz. Acquisition, relaxation, and mixing times were 0.22, 1.0, and 0.5−0.6 s, respectively. The data were collected in phase using the hypercomplex method. Eight accumulations and 256 increments were used. The final matrix had 4096 data points in *F*1 and 1042 data points in *F*2, respectively, obtained by zerofilling and linear prediction. The spectra were processed on a Sun station using Varian VNMRS 5.1 software, applying normal processing functions.

Computational Methods

Conformational analyses, molecular mechanics geometry optimization, and molecular dynamics simulations were done using MacroModel 7.1.[43] The GB/SA continuum model[44] for solvent was used throughout. Conformation searching was done using the grid search method.[45] Energy minimization was done using the AMBER* force field with no cutoff of any kind invoked and implementing a conjugate gradient minimizer using MacroModel's default convergence criteria. The molecular simulations were done using the stochastic dynamics method to simulate the random collisions with solvent as well as solvent friction forces.[46] The time step used in the numerical integration of Newton's equations was 1 fs. Initial geometry corresponded to the structure in Figure 6; to generate the diastereomeric complex, the H and the isobutyl groups attached to the stereogenic carbon of the analyte were switched, and the geometry of that structure was fully optimized prior to the

---

(42) Small, L. D.; Rosenberger, H.; Nwangwu, P. U.; Holcslaw, T. L.; Stohs, D. J. *J. Med. Chem.* **1979**, *22*, 1014−1016.

(43) Mohamadi, F.; Richardson, N. G. J.; Guida, W. C.; Liskamp, R.; Lipton, M.; Caufiled, C.; Chang, G.; Still, W. C. *J. Comput. Chem.* **1990**, *11*, 440−467.

(44) Still, W. C.; Tempczyk, A.; Hawley, R. C.; Hendrickson, T. *J. Am. Chem. Soc.* **1990**, *112*, 6127−6129.

(45) Leach, A. In *Reviews in Computational Chemistry*; Lipkowitz, K. B., Boyd, D. B., Eds.; VCH: New York, 1991; Vol. 2, pp 1−47.

(46) Gunsteren, W. F. v.; Berendsen, H. J. C. *Mol. Simul*. **1988**, *1*, 173−185.

MD protocol. A warm-up protocol beginning from 0 to 298 K was done over a time of 5 ps. The system was then equilibrated for 100 additional ps, and then a production run of 1000 ps was carried out. This heating−equilibration−simulation protocol was used for both complexes described in this paper. Details of the methodology for simulating SO/SA interaction in chromatography can be found in a previous paper.[47] Structures were sampled uniformly during 1 ns simulations and saved to disk for postprocessing (10 000 total structures for each diastereomeric complex). Postsimulation analysis of the SD trajectories was performed with an in-house program *anout*, that computes, among other properties, intermolecular energies and the center-of-mass (COM) positions of one molecule relative to another.[37]

Acknowledgment. This work was carried out by grants from the National Science Foundation CHE-9982888, the Petroleum Research Fund #35172-AC4 administered by the American Chemical Society (K.B.L.), the European Community Brite EuRam III, Project #BE 96-3159, and the Austrian Science Fund, Project #P-14179-CHE (W.L.).

Supporting Information Available: Information concerning the X-ray structure including atomic coordinates, bond lengths, bond angles, and torsion angles (PDF). This material is available free of charge via the Internet at http://pubs.acs.org.

JA020203I

---

(47) Lipkowitz, K. B. *Acc. Chem. Res*. **2000**, *33*, 555−562.